

**MATERIAL CHARACTERIZATION IN THE MICROWAVE RANGE, WHEN THE NEW MATERIALS BECOME COMPOSITE, REINFORCED, 3D-PRINTED, ARTIFICIAL, NANOMATERIALS AND METAMATERIALS (Part 2)**

PLAMEN I. DANKOV

*Sofia University "St. Kliment Ohridski", Faculty of Physics, Department of Radio-Physics and Electronics, J. Bourchier Blvd. 5, 1164-Sofia, Bulgaria*

*Пламен И. Данков, ХАРАКТЕРИЗИРАНЕ НА НОВИТЕ МАТЕРИАЛИ В МИКРОВОЛНОВИЯ ДИАПАЗОН, КОГАТО ТЕ СТАВАТ ПОДСИЛЕНИ, КОМПОЗИТНИ, 3D-ПРИНТИРАНИ, ИЗКУСТВЕНИ, НАНО- И МЕТАМАТЕРИАЛИ (Част 2)*

В първата част на тази работа ние представихме своите концепции, модели, измерителна методология и измерителни методи за екстракция на диелектричните и магнитни параметри на различни изкуствени материали, базирани на 18-годишен опит в областта на характеризирани на материалите в Микровълнова лаборатория във Физически факултет на Софийски Университет „Св. Климент Охридски“ в България. В тази 2-ра част ние продължаваме да представяме активността на лабораторията за определяне на диелектрични и магнитни параметри на различни изкуствени материали: 3D принтирани диелектрици, новата генерация подложки, керамики, многослойни антенни покрития, пенообразни материали, абсорбери, градиентни диелектрици и магнито-диелектрици, текстилни тъкани, метаматериали, С-съдържащи материали, течности, свежи растителни тъкани и пр. Специално обстоятелство е наличието на анизотропия на тези материали (различни параметри в различни посоки), която е много информативен параметър и дава ценни допълнителни данни за образците.

*Plamen I. Dankov, MATERIAL CHARACTERIZATION IN THE MICROWAVE RANGE, WHEN THE NEW MATERIALS BECOME COMPOSITE, REINFORCED, 3D-PRINTED, ARTIFICIAL, NANOMATERIALS AND METAMATERIALS (Part 2)*

In the first part of this paper, we presented a summary of our concepts, models, measurement methodologies and measurement methods for extraction of the dielectric and magnetic parameters of different artificial materials, based on 18-year experience in the material characterization in the Microwave Laboratory of the Faculty of Physics in Sofia University, Bulgaria. In this part, we continue to present the activity of this laboratory for characterization of the dielectric and magnetic parameters of different artificial materials: 3D printed dielectrics, reinforced substrates, ceramics, antenna radomes, foams, absorbers, gradient dielectrics and magneto-dielectrics, textile fabrics, metamaterials, carbon-content materials, liquids, fresh plant tissues, etc. A special circumstance is a dielectric anisotropy of these materials (different permittivity in different directions), which is very informative parameters and gives valuable additional data for the samples.

***Keywords: 3D printed dielectrics, anisotropy, artificial dielectrics, ceramics, conductivity, metamaterials, microwave measurement methods, permeability, permittivity, textile fabrics***  
***PACS numbers: 77.22.-d***

*For contact: Plamen Dankov, Sofia University "St. Kliment Ohridski", Faculty of Physics, 5, J. Bourchier Blvd., 1164-Sofia, Bulgaria [dankov@phys.uni-sofia.bg](mailto:dankov@phys.uni-sofia.bg)*

## 1. INTRODUCTION

We considered in the first part of this review paper [1] the activities of the Laboratory for Microwave material characterization in Faculty of Physics, Sofia University “St. Kliment Ohridski”, Bulgaria, orientated to a determination of the dielectric and magnetic properties of the modern artificial materials in microwave range: 3D printed dielectrics, reinforced substrates, multilayer composites, thin films, metamaterials, etc. A special circumstance is the existence dielectric/magnetic anisotropy of these materials (different permittivity and permeability along different sample directions), which is more informative parameters than the simple determination of the scalar material constants and could be bound with the sample composition, sizes, structure, inclusions’ orientation, technology, conditions for sample preparation and other technological processes. In our 17-year research work, we realized this advantage for knowledge of possible anisotropy properties for more complete and valuable material characterization.

Referring to the first part [1] for the modern materials’ classification and discussion the origins for appearing of artificial anisotropy in most of them, we concentrate our efforts to a characterization of the dielectric/magnetic anisotropy of these artificial materials, where this property could be considered more as undesired, but unavoidable characteristic, which should be taken into account in the modern 3D design of different structures and devices for the microwave electronics and applications in the 5G communication standard, especially at higher frequencies. In [1], we described the developed and realized in our laboratory a set of numerical and measurement methods for characterization of the material parameters in the microwave range (0.5-40 GHz), anisotropy and procedures for reliable extraction of the material parameters from the obtained measurements results on the base of analytical models or specific techniques for utilization of the commercial 3D electromagnetic simulators as auxiliary tools for extraction of sample parameters. In the second part, we illustrate our rich experience in the area of material characterization by presenting a lot of published and new results for determination of the dielectric (and magnetic) parameters and specific properties of many commercial and unique artificial materials: new generation of microwave reinforced substrates, specially developed for 5G applications, ceramics and other crystalline samples, multilayer radomes, foams, absorbers, gradient dielectrics and magneto-dielectrics, textile fabrics, 3D printed dielectrics, metamaterials, carbon-content materials, composites, liquids, powders, fresh plant tissues, plasmas, ferrites, etc.

## 2. DIELECTRIC PROPERTIES AND ANISOTROPY OF REINFORCED, IMPREGNATED, WOVEN, KNITTED AND OTHER FIBRE MATERIALS

The dielectric mixtures based on two or more dielectrics, one part of them performed as reinforcing filaments (fibres, threads, yarns) and another part – as appropriate fillers (ceramics, PTFE, epoxy resins, air, etc.), are very popular in

the modern electronics –see Fig. 2.1. This is a group of useful artificial materials, which can be used as substrates for printed circuit boards (PCB), reinforcing skins and foam cores for multilayer antenna radomes, textile fabrics, used for wear-able antennas, self-reinforcing plastics, etc. The most spread of them is the group of *reinforced PCB substrates* as commercial products (considered in §2.1). They consist of woven or nonwoven reinforcing fibre-glass fabrics and different fillers and the resultant homogenized structures can be used in different parts of the microwave range. Nowadays some traditional *textile fabrics* also can act as substrates for the popular wearable antennas in the new communication body-area networks (§2.2). Another variant of the reinforced *epoxy-glass laminates* is applicable for antenna radomes and other radio-transparent and mechanically stable constructions (§2.3). Multilayer and gradient absorbers (§2.4) are also artificial materials, which could be added to this group.

Of course, the question that must be answered when designing such composites is how to predict the effective/equivalent dielectric properties of the whole system (note that similar approaches should be applied also to the mechanical and thermal properties)? We already considered (§2.2 in [1]) several closed-form expressions for analytical determination of the equivalent complex dielectric constant of different mixtures (early concepts [3] and some new approaches for 2-D [4, 5] or 3D [6] woven fabrics, including the numerical techniques [7]). To obtain the required information for the resultant dielectric mixture, it is necessary to estimate the permittivity of the separate constituents (phases) and the used mixture topology. Finally, appropriate measurements of the resultant complex dielectric constants are also necessary to be performed by destructive or nondestructive methods (already presented in [1], §3).

The topology of the considered reinforced dielectric mixtures (shown in Fig. 2.1) suggests the existence of artificial anisotropy, caused by the spatial inhomogeneity in different directions between the mixed reinforcing fibres and the filling. We already discussed in [1] its origin (§2.3) and developed authorship methods for numerical and experimental determination of the anisotropy of such materials. We use the following expressions for anisotropy characterization (for dielectric constant and dielectric loss tangent; parameters  $\Delta A_\varepsilon$ ,  $\Delta A_{\tan\delta\varepsilon}$ ):

$$\Delta A_{\varepsilon,0x/y} = 2(\varepsilon'_{0x/y} - \varepsilon'_{0z}) / (\varepsilon'_{0x/y} + \varepsilon'_{0z}), \quad (8.1)$$

$$\Delta A_{\tan\delta\varepsilon,0x/y} = 2(\tan\delta_{\varepsilon,0x/y} - \tan\delta_{\varepsilon,0z}) / (\tan\delta_{\varepsilon,0x/y} + \tan\delta_{\varepsilon,0z}), \quad (8.2)$$

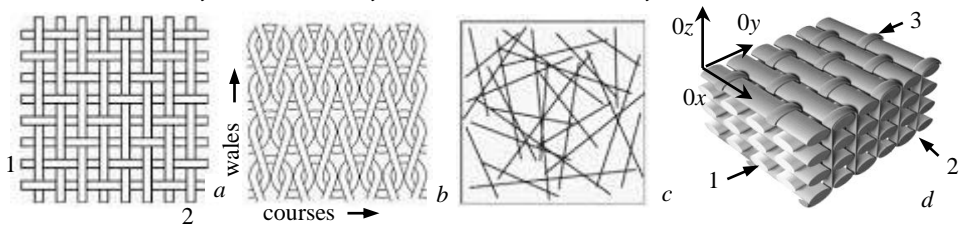


**Fig. 2.1** Examples for some filament mixtures: *a*) 2D woven fabrics; *b*) Jersey knitted fabrics; *c*) non-woven fabrics; *d*) 3D woven composites (legend: 1 – warp yarn; 2 – weft yarn; 3 – Z-yearn)

where  $\epsilon_{0x}$ ,  $\epsilon_{0y}$  and  $\epsilon_{0z}$  are the real dielectric constants, while  $\tan\delta_{\epsilon,0x}$ ,  $\tan\delta_{\epsilon,0y}$  and  $\tan\delta_{\epsilon,0z}$  are the dielectric loss tangents (dissipation factors) along the axes  $Ox$ ,  $Oy$  and  $Oz$  (as shown in Fig. 2.1d). The considered case refers to the bi-axial anisotropy (for a pair of three different components along each axis). When the parallel components according to substrate surface coincide (i.e.  $\epsilon_{0x}=\epsilon_{0y}=\epsilon_{par}$  and  $\epsilon_{0z}=\epsilon_{perp}$ ;  $\tan\delta_{\epsilon,0x}=\tan\delta_{\epsilon,0y}=\tan\delta_{\epsilon,par}$  and  $\tan\delta_{\epsilon,0z}=\tan\delta_{\epsilon,perp}$ ), the uni-axial anisotropy takes place. In the next four sections, we will consider the specific features and peculiarities of the considered types of dielectric mixtures and their anisotropy.

## 2.1. REINFORCED SUBSTRATES

The reinforced substrates are key materials in modern electronics – the basis for the realization of new devices by microwave integrated circuits (MICs) and especially for the last 5G communication standard. These materials consist of reinforcing fibre-glass fabrics and a variety of fillers – see Fig. 2.2. This mixture is a classic example for uni-axial anisotropic materials: usually, the glass fibres are high-permittivity supports, while the fillers – low-permittivity homogenizing media (with some exceptions, when the fillers are high-permittivity ceramic powders). Due to this combination of constituents the parallel dielectric constant (along the glass fibres) is usually bigger than the perpendicular one, i.e.  $\epsilon_{par} > \epsilon_{perp}$  (the behaviour of the textile fabrics with air filling is very similar; see §2.2)

The main role of the substrate is to support the metallic layout and surface-mounted components of the PCB schemes; however, in the microwave range, the substrate dielectric properties influence the electrodynamic behaviour of the whole printed structure. Thus, a reliable determination of the dielectric parameters of each commercial substrate by the manufacturers is very important for the consumers. The producers apply the reference IPC TM-650 2.5.5.5 test method [8] (based on clamped stripline resonator), which gives  $Oz$  dielectric constant and dissipation factor, denoted with the popular in the datasheets symbols  $Dk$  and  $Df$  and this pair of two values is usually enough for many applications at lower frequencies (for example, in planar schemes on the popular epoxy-glass laminate FR-4 [9], manufactured by many companies). However, at higher frequencies the anisotropy becomes important, especially for mmMICs, working in the mm-wavelength range, because the wavelength becomes compatible with the spatial

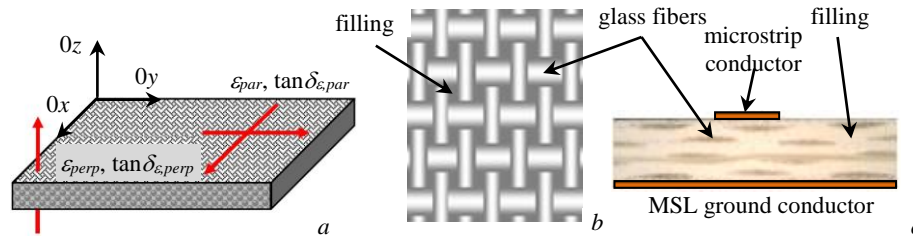


**Fig. 2.2.** Schematic view of the reinforced substrates: *a*) substrate with uni-axial anisotropy; *b*) top view (glass fibre fabrics and fillers); *c*) side view of a microstrip line on reinforced substrate

irregularities in the reinforced substrate (well-illustrated in Fig. 2.2c)

As we mentioned in [1], we maybe were the first researchers (based on our experience with ferrites and ceramics), which detected the dielectric anisotropy of several popular commercial reinforced substrates in 2000-2002 by the developed authorship two-resonator method [1] and published the first paper [A8]. For example, we measured for one commercial substrate Ro3203 (0.254-mm thick; 10 mils) considered as isotropic:  $\epsilon_{par} \sim 3.238$ ,  $\epsilon_{perp} \sim 3.036$  (reference value 3.02 [10]), equivalent dielectric constant  $\epsilon_{eq} \sim 3.111$  in the X band and dielectric anisotropy  $\Delta A_\epsilon \sim 6.4\%$  (indeed the term “equivalent dielectric constant” was firstly introduced exactly in this paper). We presented also results for other popular substrates (e.g. for the practical isotropy of Ro3003, RT Duroid 6002; useful data for Ro4003, FR-4, etc.), but due to the used perturbation approximation for TM-mode resonator, some of the obtained results were not so accurate, especially for thick substrates. Then we developed more accurate full-wave analytical models and later on effective numerical techniques of the measurement resonators and extraction procedures for determination of the parameters Dk/Df of uniaxial anisotropic single and multilayer samples by the two-resonator method (see [1] and [A18, A22, A27, A32]). In a relatively short period (2004-2008) we succeeded to accumulate useful data for the real anisotropy on many commercial substrates from different manufacturers and had the unique possibilities to compare and to publish some of them. In our practice we met commercial substrates with different degree of anisotropy: 1) near-to-isotropic ( $\Delta A_\epsilon < 2-3\%$ ; non-woven substrates); 2) substrates with middle anisotropy ( $\Delta A_\epsilon \sim 5-11\%$ ; the most typical case) and 3) relatively big anisotropy ( $\Delta A_\epsilon > 15-20\%$ ) [A32]. Today we can distribute in each group many well-known commercial products on the base of our measurements, but this information is very sensitive for the most manufacturers and we try to use in our recent publications virtual denotations instead the real substrate names (as in [1]), when the substrates are still on market. The large companies continue to support an opinion that the anisotropy of part of their products is “a bad property” for the consumers (although it is a completely natural property for such mixtures) and they usually don’t comment the measured anisotropy effects in details, nevertheless that the degree of this anisotropy directly depends on the applied technology. Until 2006 we didn’t manage to find any information about the anisotropy of commercial substrates published in the official specifications. However, in this period, 2002-2005, we found out several articles (not cited), presented on the largest microwave conferences, where the authors disagree with some reference Dk data. For example, some of them have assumed a value of  $\sim 3.52$  for Dk of the very popular at that time substrate Ro4003 instead the catalogue value 3.38 (4.1-% increase!). They explained this decision with “better results obtained during the simulations of MSL filters on this substrate”. It was a strange explanation for us; users, who typically draw the geometrical structures of the designed planar devices in the simulators with extremely large details, frivolously start to adjust the substrate Dk value in their

projects until the simulation results coincide with the measurement ones (!). For information, in this period we measured the following Dk values for Ro4003 (0.508-mm thick; 20 mils):  $\epsilon_{par} \sim 3.66$ ,  $\epsilon_{perp} \sim 3.37$  (close to catalogue value 3.38), equivalent dielectric constant exactly  $\epsilon_{eq} \sim 3.52$  for 50-Ohms microstrip lines (MSL) in the Ku band; i. e. a moderate dielectric anisotropy  $\Delta A_\epsilon \sim 8.3\%$ . Other research groups also started to show their results for anisotropy of different substrates (see the references in [1])

Step by step, the large PCB manufacturers accepted the problems with substrate anisotropy and offered solutions to overcome them, but without to discuss in details the problems' source. The first company, according to us, which officially shared information for measured dielectric anisotropy of its substrate, was Taconic Headquarters Ltd., Advanced Dielectric Division. In paper [11] the authors started to discuss the dielectric anisotropy of their material TLY-5A (measured by Bereskin's method [12]). As early as 2012, the next company that began to share results for the measured anisotropy of some of its products was Rogers Corp. Ltd. In the paper [13] the company researchers presented relatively detailed information for the anisotropy of some their substrate; even adduced a discussion for the obtained results, published earlier in our papers. They confirmed all our results, excepting data for one substrate with high-Dk. In 2013, Isola Group Ltd. also started to discuss and to solve the problems with substrate anisotropy, especially at higher frequencies (for substrates with 5G applications) and shared information for the equivalent dielectric constant [A42]. The concept for the equivalent dielectric constant, when the anisotropic substrate can be replaced with isotropic one, was more or less implemented in the datasheets. For example, Rogers Corp. (and then practically all other large PCB manufacturers: Taconic, Isola Group, ITEQ Corp., Shengyi Technology Co, etc.) started to give so-called design Dk value of each RF substrate (together with the reference technological Dk value obtained by IPC-TM-650 2.5.5.5 method) to ensure optimum simulation results. The large software developers also added the corresponding design Dk values in their material tutorials. Strictly speaking, the parameter design Dk was not well validated in the beginning, but the recent publications from the company researchers (e.g. [14]) discuss the problems of the substrate anisotropy and give unpublished data for many products. Nowadays, most of the companies present three Dk values (but not for all products): technological Dk (close to  $\epsilon_{perp}$ ); design Dk (close to  $\epsilon_{eq}$  for MSL) and a value, obtained by SPDR method (close to  $\epsilon_{par}$ ), which completely correspond to our concept for the reinforced substrates, developed since 2000 (see [1], §3.3). This information helps to solve the problems with substrate anisotropy: producers try to have "a full 3D dielectric picture" of their products in order to have better control on technology, while RF engineers would like to perform the better 3D design of their devices.

Therefore, we can conclude that the development of measurement methods for determination of the important dielectric parameters of commercial substrates, especially in the mm-wavelength range, is substantial and we continue to

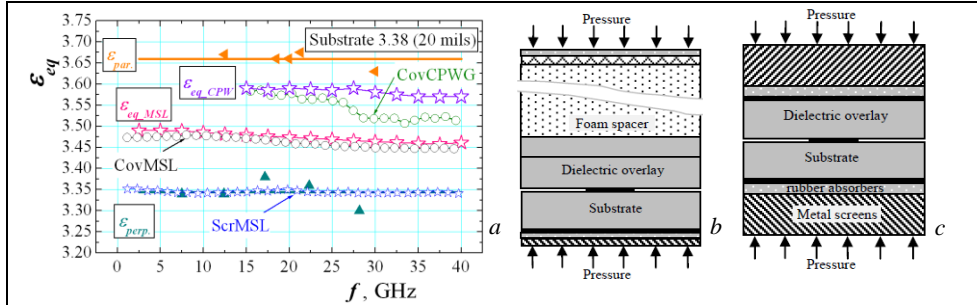


**Fig. 2.3.** *a)* Comparison between the frequency dependencies of the equivalent dielectric constant  $\epsilon_{eq}$  for uncovered and covered MSL and CPW, compared with  $\epsilon_{par}$  and  $\epsilon_{perp}$  values of “Substrate 3.38”; *b)* covered MSL line resonator (side view) for direct measurement of  $\epsilon_{eq}$ ; *c)* screened MSL line resonator (quasi-IPC method) for direct measurement of  $\epsilon_{perp}$  up to 40 GHz [A46]

develop new methods (see also [1]). For example, in our paper [A46] we have presented new methods for direct measurements of the two important substrate parameters by direct determination of effective  $\epsilon_{eff}$ : design Dk (by covering of MSL with enough thick overlay from the same material) and technological Dk (by an appropriate screening of MSL) – see Fig. 2.3. The measurements of close to parallel Dk by covering of CPW were also successful [A47, A60-A64].

Of course, our main advantage in the process for characterization of all accessible on the market commercial substrates is the possibility really to obtain a full 3D “portrait” of the dielectric properties of these important materials, measuring the anisotropy by our two-resonator method [A22, A27, A32] and equivalent parameters, when these materials have been considered as isotropic ones [A32, A44]. This information can help many users to perform the better and reliable design of different planar structures on these substrates, especially in the mm-wavelength range and the manufacturers to have better technology control of their products. Fig. 2.4 presents the photography of a set of eight TE- and TM-mode resonators, which “covers” the frequency interval 5-39 GHz by applying the fundamental modes in each resonator (and even up to 80 GHz by applying appropriate high-order modes). Using this measurement tool and its modifications [1], we managed to characterize more than 50 different substrates, accessible on the world market; a small part of the obtained results (<10 %) have



**Fig. 2.4.** Pairs of optimized measurement resonators with different diameters: *a)* TE-mode R1 (30, 18, 15, 10 mm) and *b)* TE-mode R2 (30, 18, 10, 8 mm), which cover frequency range 5-39 GHz

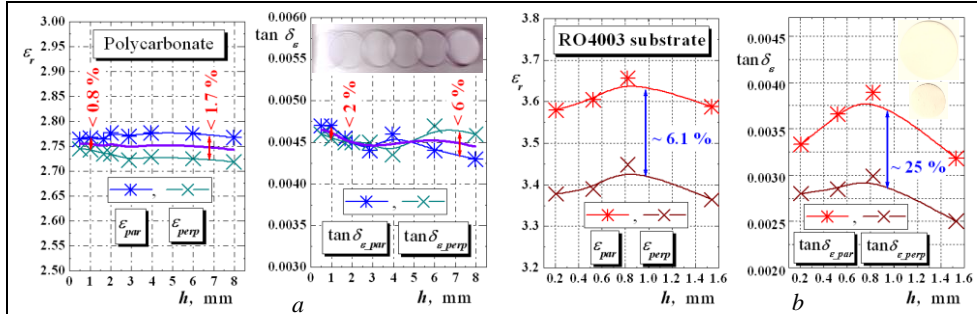


**Fig. 2.5.** One of our first results (taken from Chapter [A32]) for measured dielectric parameters  $v/s$  thickness of the isotropic Polycarbonate (a) and a popular commercial substrate Ro4003 (b)

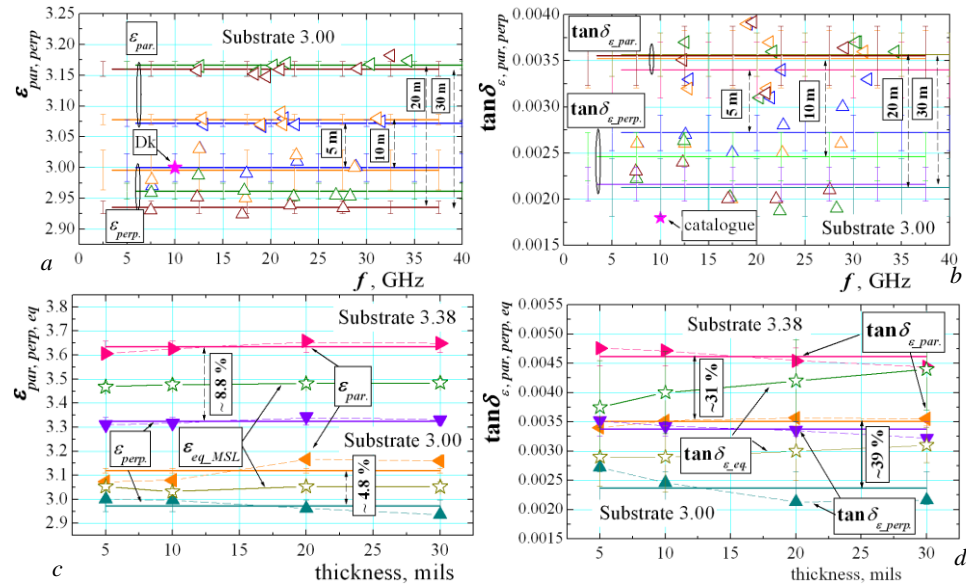


**Fig. 2.6.** 3D portrait of dielectric anisotropy of two commercial substrates conditionally marked as Substrate 3.00 ( $Dk = 3$ ) and 3.38 ( $Dk = 3.8$ ), versus frequency (a) and thickness (b)

**Table 1.** Measured dielectric parameters and anisotropy of some commercial substrates, which catalogue parameters are practically equal or very similar

Substrate	$h$ , mm	parallel $\epsilon_{par}/\tan\delta_{par}$	perpendicular $\epsilon_{perp}/\tan\delta_{perp}$	equivalent $\epsilon_{eq}/\tan\delta_{eq}$	$\Delta A_{\epsilon}/\Delta \tan\delta_{\epsilon}$ , %	IPC TM 650 2.5.5.5 @ 10 GHz
Rogers Ro4003	0.510	3.67/0.0037	3.38/0.0028	3.53/0.0031	8.2/27.7	3.38/0.0027
Arlon 25N	0.520	3.57/0.0041	3.37/0.0033	3.37/0.0033	5.8/21.6	3.38/0.0025
Isola 680	0.525	3.71/0.0049	3.32/0.0042	3.32/0.0042	11.1/15.4	3.38/0.0030
Neltec NH9338	0.520	4.02/0.0051	3.14/0.0025	3.51/0.0032	24.6/68.4	3.38/0.0025
Rogers Ro3003	0.27	3.00/0.0012	2.97/0.0013	2.99/0.0013	1.0/-8.0	3.00/0.0013
Rogers Ro3203	0.26	3.18/0.0027	2.96/0.0021	3.08/0.0025	7.2/25.0	3.02/0.0016
Neltec NH9300	0.27	3.42/0.0038	2.82/0.0023	3.02/0.0023	19.2/49.2	3.00/0.0023
Arlon DiClad880	0.254	2.32/0.0016	2.15/0.00093	2.24/0.0011	7.6/53.0	2.17/0.0009

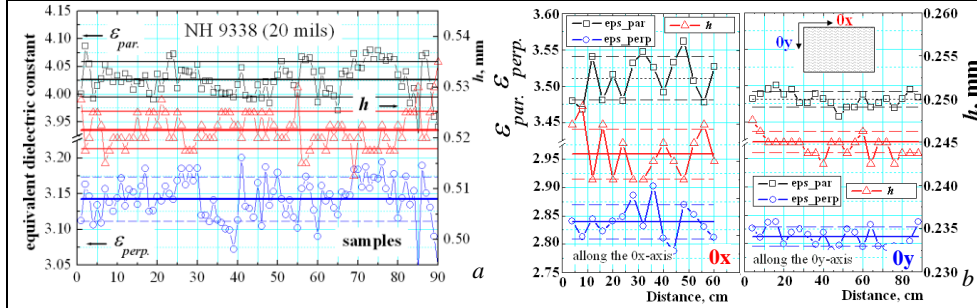


**Fig. 2.7.** Statistical data for substrate NH 9338 (a) and its parameters' inhomogeneity (b) [A14]

**Table 2.** Measured standard deviations for parameters of large-size substrate sheets [A14]

Substrate	SD $\epsilon_{par}$	SD $\epsilon_{perp}$	SD $\tan\delta_{epar}$	SD $\tan\delta_{eperp}$	SD $h$	Samples number	SD $\epsilon_{eff}$	SD $\beta$	SD $\alpha$	
										SD $\epsilon_{eq}$
Ro4003	$\pm 0.2$	$\pm 0.5$	$\pm 2.0$	$\pm 9.0$	$\pm 0.2$	32	$\pm 0.22$	$\pm 0.45$	$\pm 0.23$	$\pm 4.4$
NH9338	$\pm 0.8$	$\pm 1.0$	$\pm 8.5$	$\pm 13.0$	$\pm 0.7$	90	$\pm 0.52$	$\pm 0.91$	$\pm 0.45$	$\pm 6.1$

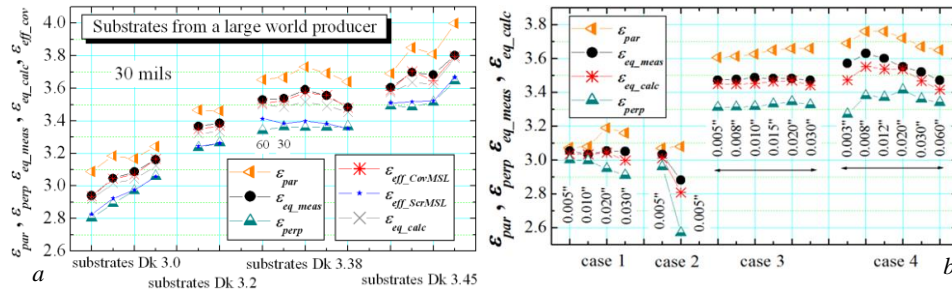


**Fig. 2.8.** Examples for measured parallel, perpendicular and equivalent dielectric constant of different commercial substrates: a) for different products of one company; b) Comparison: case 1) low-Dk (~3.0) substrate with minimized anisotropy for small thickness; case 2) two low-Dk substrates with different anisotropy; cases 3, 4) family of substrates with Dk~3.38 from two different companies covering a wide thickness range 3-60 mil [A48]

been published with the actual substrate names (e.g. as in [A32]) – as in Fig. 2.5 and Table 1. The other unpublished part composes our rich database for many substrates, including the last products. We can characterize the separate substrate materials in several ways [A37, A42]. The first two ways are based on obtaining information for the anisotropy of commercial substrates versus the frequency (as in Fig. 2.6a,b) and thickness (as in Fig. 2.6c,d or Fig. 2.5b). The set of averaged values of parameters  $\epsilon_{par}$ ,  $\epsilon_{perp}$ ,  $\epsilon_{eq}$  and  $\tan\delta_{epar}$ ,  $\tan\delta_{eperp}$ ,  $\tan\delta_{eq}$  gives valued information for each substrate and allows comparison between substrates from a specific group (like examples in Table 1), which is important for the producers and useful for the users. The last two ways for obtaining of substrate parameters are difficult – statistical data, extracted from a large number of samples (as in Fig. 2.7a) and information for dielectric parameters inhomogeneity in large-size substrate sheets (Fig. 2.7b). Such data, compared for a set of several concurrent substrates, are decisive for the right choice of the bigger users of these materials

because they show the stability of the dielectric parameters and parameters of the constructed on their base devices – e.g. impedance  $Z_c$ , propagation constant  $\beta$  and attenuation  $\alpha$  (see Table 2). Fig.2.8 illustrates well how we can use our database for substrate parameters. A set of parameters and anisotropy of different 30-mils substrates of one producer is presented in Fig. 2.8a with typical dielectric constants 3-3.8. Fig.2.8b (1,2) illustrates the attempts of one producer to minimize the anisotropy of low-Dk substrates with applicability in the mm-wavelength range; while Fig. 2.8b(3,4) gives a useful comparison between a family of similar products of two companies with  $Dk \sim 3.38$  for different thickness.

## 2.2. TEXTILE FABRICS FOR ANTENNA APPLICATIONS

The textile fabrics show quite similar behaviour of the dielectric properties and anisotropy like the reinforced substrates due to the structures' resemblance. In our first publications on this topic [A49, A51] we presented measured by the two-resonator method dielectric anisotropy of several most popular natural and synthetic textile fabrics (see also selected results in Table 3). It turned out that the actual anisotropy  $\Delta A_\epsilon$  of textiles is small (1.5-5%) or moderate (5-9%) as the wide-spread commercial reinforced substrates (compare with data in Table 1). Only for more complex and multilayer artificial fabrics, the anisotropy  $\Delta A_\epsilon$  exceeds 10-12%. Then, in paper [A51] we developed 3D models for the numerical determination of dielectric anisotropy of woven and knitted textile fabrics (Fig. 2.9) and presented useful results (part of them shown in Table 4) (see also considerations in §2.4 in [1]). The information for the anisotropy of these artificial fabrics confirms the rule that the dielectric constant of these air-filled dielectric mixtures increases in the direction parallel to the axes of fibres and decreases in the perpendicular direction (that why, different sample anisotropy  $\Delta A_\epsilon$  appears from  $\pm 5\%$  up to 12-18% – last column in Table 4). These results give ideas on how to minimize the undesired anisotropy of these materials (including also

**Table 3.** Measured dielectric parameters and anisotropy of some classical textile fabrics (averaged values for frequency interval 0-36 GHz) [A64]. Insets at right: different disk textile samples

Textile fabric	$t$ , mm	$\epsilon_{par}$ / $\tan\delta_{\epsilon_{par}}$	$\epsilon_{perp}$ / $\tan\delta_{\epsilon_{perp}}$	Anisotropy $\Delta A_\epsilon/\Delta A_{\tan\delta_\epsilon},\%$
Epoxy-based waterproof fabric	0.35	1.97/0.010	1.83/0.007	7.4/30
Waterproof fabric with breathability GORE-TEX® [16]	0.20	1.53/0.006	1.38/0.004	10.3/28
Weaved silk	0.19	1.60/0.028	1.54/0.016	3.8/57
Weaved linen	0.65	1.65/0.043	1.58/0.044	4.3/-2.3
Weaved hemp fishnet	0.81	1.63/0.072	1.43/0.034	13.1/72
Natural leather	0.84	2.47/0.055	2.44/0.054	1.2/1.8
Weaved wool	2.10	1.28/0.026	1.21/0.015	5.6/54
Jersey knitted wool	5.50	1.40/0.024	1.26/0.021	10.5/13.3
Denim	0.93	1.69/0.027	1.61/0.030	4.8/-11
Cotton satin 5	0.25	1.58/0.019	1.45/0.013	8.6/38
Jersey knitted cotton	0.40	1.56/0.055	1.50/0.044	3.9/22.2



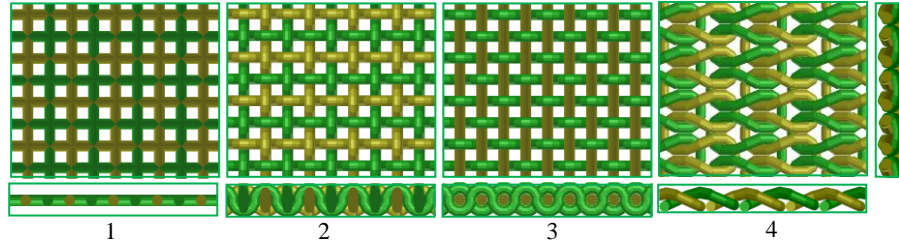


**Fig. 2.9.** Top and side views of 3D models of four artificial materials, made by straight or meander yarns with diameters 0.5 mm and distance between their centres 1 mm (the unit cell of samples is  $1 \times 1 \times 1.5$  mm; the unit cell has been repeated only in the  $Oxy$  plane)

**Table 4.** Simulated dielectric parameters and anisotropy of several artificial textile structures

No	Sample description	$\epsilon_{par}$ $/\tan\delta_{\epsilon_{par}}$	$\epsilon_{perp}$ $\tan\delta_{\epsilon_{perp}}$	Anisotropy $\Delta A_{\epsilon}/\Delta A_{\tan\delta_{\epsilon}}\%$
1	Straight cylinders along to $0x$ and $0y$ direction (fish net)	1.432/0.0020	1.205/0.0005	17.2/120
2	Meander cylinders along to $0x$ and $0y$ directions (woven symmetrical net)	1.673/0.0022	1.750/0.0025	-4.5/-12.4
3	Meander cylinders along to $0x$ direction and straight cylinder along to $0y$ directions	1.593/0.0022	1.519/0.0017	4.8/22.8
4	Jersey knitted fabric	1.726/0.0026	1.530/0.0015	12.0/53.7

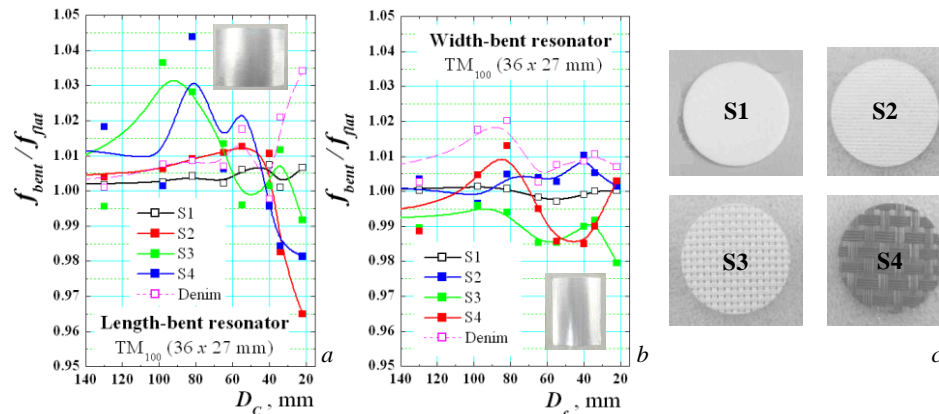


**Fig. 2.10.** Measured normalized resonance frequencies of length-(a) or width-bent (b) rectangular resonator  $36 \times 27$  mm on substrates S1, S2, S3 and S4 (c) with measured anisotropy  $\Delta A_{\epsilon} \sim 0.4$ ; 5.7, 13.7 and 11.3 % correspondingly [A64].

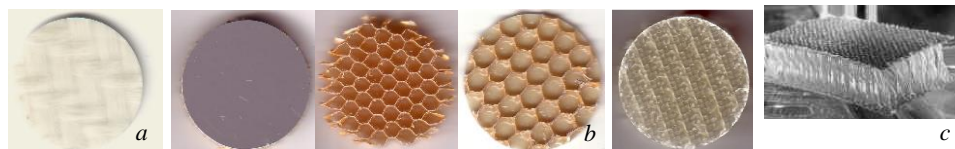
reinforced substrates). In [A51] we investigated the behaviour of microstrip patch antennas and arrays on anisotropic textile substrates (frequency band, beam-width, directivity and efficiency). In the recent paper [A64] we continued this research with bent microstrip rectangular resonators on selected substrates with different anisotropy. We found out that the resonance frequencies of the dominant mode in these bent structures (Fig. 2.10) depend not only on the curvature diameter  $D_c$  (obtained for pure isotropic substrates like S1) but also on the concrete anisotropy  $\Delta A_{\epsilon}$  (for samples S2, S3, S4) (or combination between  $D_c$  and  $A_{\epsilon}$ ), which is a completely new result (the research is still in progress).

### 2.3. MULTILAYER ANTENNA RADOMES

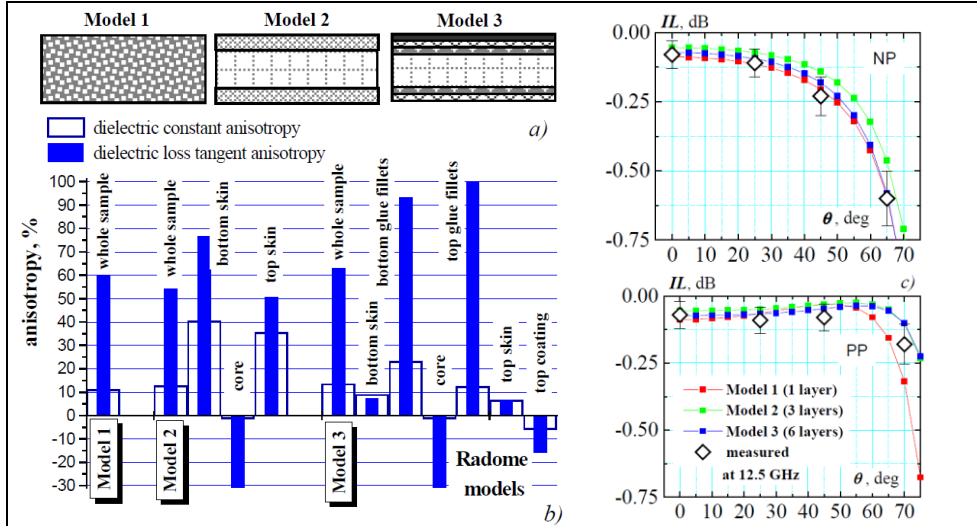
Antenna radomes are very important structures in the antenna design: they ensure the mechanical and weather stability of different open-air antennas and, at the same time, they should be radio-transparent in the used frequency ranges. Therefore, the proper radome design separately from (or together with) the antenna design is an important task, because this structure adds losses and phase delay and influences the antenna beam-forming and beam directivity. There exist two main types of radomes: thin (with thickness  $t_R$  smaller than the wavelength  $\lambda$ ) and resonance radomes (when  $t_R \sim \lambda/2$ ). The modern radomes are usually multi-layer (sandwich-type) structures. They consist of relatively thick middle core and two thin skin layers, which ensure the mechanical hardness. The cores are foams, wadding with air pores, honeycombs or similar low-Dk layers. On the contrary, the skins are reinforced layers: glass fabrics with resin epoxy filling, both with higher Dk. To perform reliable radome design, the dielectric properties of all radome layers have to be well determined. However, the considered structures of cores and hard skins definitely show that they are more or less anisotropic materials. Exactly considering these needs to determine the own anisotropy of radome layers, we developed the author-ship two-resonator method for multi-layer samples, as it is described in [A22] (see also §2.4 in [1]).

Fig. 2.11 presents three examples of antenna radomes. The single-layer reinforced thin radome (Fig. 2.11a) could be considered as a reinforced substrate (§2.1). The popular three-layer honeycomb radome consists of rare honeycomb core (e.g. Kevlar® paper) and two different (top and bottom) skin layers – thin glass-fibre fabrics with resin filling – Fig. 2.11b. All these samples have expressed anisotropy, illustrated in Fig. 2.12b. Based on these data we can construct different radome models – with one, three or six layers (Fig. 2.12a) (the last model includes two additional thin layers formed by the glue residues between the core and skins and a coating layer). We developed in our papers [A15, A20] an analytical model for determination of radome insertion (IL) and return (RL) losses of multilayer samples with anisotropy on the base of Paris' model [16] for isotropic multilayer radomes. The comparison (Fig. 12c) between the numerical and measured IL fully confirms the validity of our theoretical radome model.

The third example is very interesting from a measurement point of view – Fig. 2.11c. We proposed for the first time in [A22, A26] the commercial Para-



**Fig. 2.11.** Samples from radomes: a) reinforced TWINTEX® fabrics woven with commingled E-glass and polypropylene filaments; b) honeycomb radome: painted skin layer, Nomex® Kevlar-paper core and E-glass skin with glue residues [A20]; c) Parabeam® 3D glass fabrics: reinforced 3D woven filaments with resin filling [A26]



**Fig. 2.12.** *a)* Illustrative pictures of the used radome models with 1, 3 and 6 layers; *b)* dielectric anisotropy of separate layers and whole sample for each model; *b)* IL-dependencies versus the incident angle  $\theta$  at 12.5 GHz for multi-layer honeycomb radome with total thickness 5.5 mm for normal (NP) and parallel (PP) polarization of the incident wave

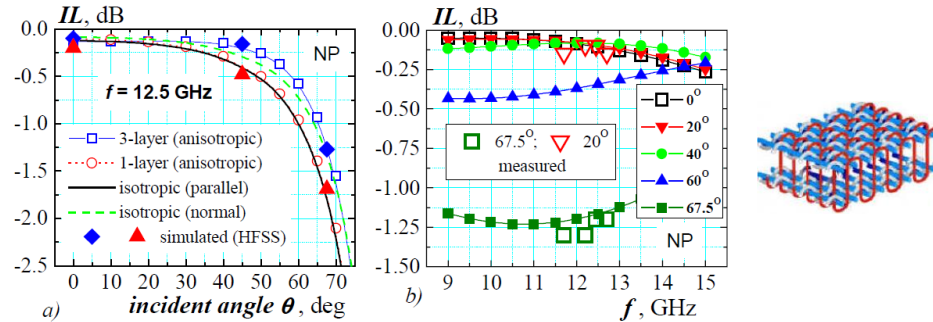


**Fig. 2.13.** Dependencies of the insertion losses IL in Parabeam® 3D glass radome [A26]: *a)* versus the incident angle at 12.5 GHz; *b)* versus the frequency at several incident angles. The results are compared with Ansoft® HFSS simulations for 1-layer and 3-layer anisotropic radome models. The measured data are obtained by measurements of the received signal in DBS-TV steerable antenna array with and without covering radome in the Ku band. Inset: radome 3D glass fabric

Beam® 3D glass fabrics to be used for antenna radome. The specificity here is the fact that the radome body is one sample: 3D glass fabric impregnated with epoxy resin and the skin layers and core are formed by a single process. Therefore, we cannot directly measure the core parameters. For this purpose we presented in [A22] a de-embedding procedure for the extraction of dielectric parameters of the middle layer: 1) characterization of parameters of the whole sample; 2) characterization of both skin layers and 3) extraction of the parameters of the inaccessible for direct measurements 3D glass core. The measured layer anisotropy is high:  $\Delta A_\epsilon \sim 27\%$  for the top smooth skin layer;  $\sim 45.7\%$  for

the rough bottom skin layer and  $\sim 5.6\%$  for 3D glass core. With the help of the constructed radome model, we determined the IL in radome for an incident wave with normal polarization (Fig. 13) versus incident angle and frequency. Simulated and measured losses practically coincide. In [A26] for the first time we presented also well-developed 3D models for effective simulations for multilayer anisotropic radomes – see illustrations in Fig. 2.14. The free-space model between two rectangular open-end waveguides gives applicable results, but with very time-consuming simulations. On the contrary, stylized models with plane-wave source allow faster simulations at different incident angles with satisfactory accuracy; however, an extraction procedure has to be applied for the determination of the insertion losses and phases due to the multilayer radome [A26].

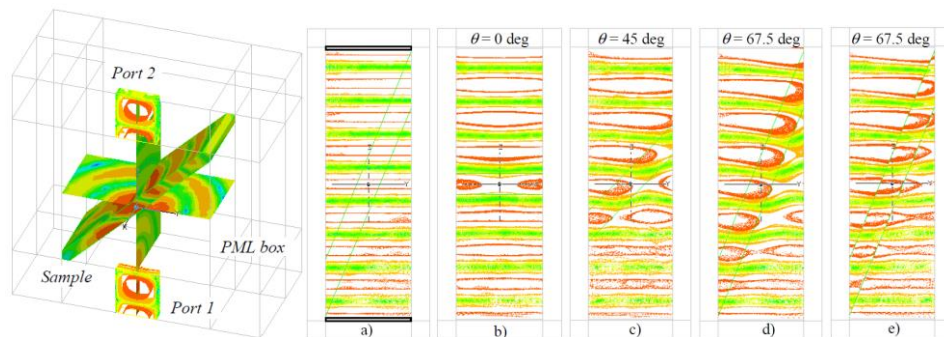


**Fig. 2.14.** (at left) Half part of a large simulated structure: radome sheet between two open-end waveguides; (at right) Incident (a) and total E field in PML box with radome, illuminated by plane wave – normal NP (b, c, d) and parallel PP (e) polarization

#### 2.4. MULTILAYER AND GRADIENT ABSORBERS

Other important materials widely used in the microwave range are microwave absorbers. Their main role in the structures, where they have been incorporated, is to suppress the parasitic interferences, cross-talk interactions and reflections. Recently, the microwave engineers started to design the whole microwave devices together with incorporated absorbers; therefore they need to know the actual electromagnetic parameters of these materials. Usually, the microwave absorbers have been offered as foams, rubber sheets, brushed coatings or thin films with absorbing inclusions (recently absorbing metamaterials). They consist of carbon, carbonyl iron, ferrites and other high-loss inclusions; therefore, they may have as pure dielectric properties (like the carbon-content absorbers), as well as magnetic properties [17]. In [A11, A16, A17, A67] we presented our attempts to determine the dielectric and magnetic parameters of thin microwave absorbers. Unfortunately in this period, the commercial absorbers' producers presented in the corresponding catalogues only data for the absorbing abilities (trough sample in dB/mm), but not the actual dielectric and magnetic constants and loss tangents. In our review paper [A28] we summarized and compare the possible methods for characterization of microwave absorbers, considered also

in [1]. There are no problems with dielectric absorbers; it is difficult to separate the magnetic and dielectric properties of samples. It is relatively easy [18] by measurements of the resonance parameters of exited  $TE_{10p}$  modes in rectangular resonators with small prism samples; first modes with odd  $p$ -values (1, 3, 5) will ensure extraction of dielectric parameters  $\epsilon_r$ ,  $\tan\delta_\epsilon$ , while first modes with even  $p$ -values (2, 4, 6) – magnetic parameters  $\mu_r$ ,  $\tan\delta_\mu$ . Fig. 2.15a presents measured dielectric  $\epsilon_r$  and magnetic  $\mu_r$  constants by perturbation methods, while Fig. 2.15b compares the product  $\epsilon_r \times \mu_r$ , obtained by different measurement methods. As an example, we give the parameters of commercial rubber absorber FM8 (Collector Magma, Slovenia) in Ku band:  $\epsilon_r \sim 18.0$ ;  $\mu_r \sim 1.5$ ,  $\tan\delta_\epsilon \sim 0.2$ ;  $\tan\delta_\mu \sim 1.0$ . Thick absorber samples cannot be well characterized by resonance methods due to the big losses. However, we proposed in [A63] a procedure for separate extraction of dielectric and magnetic parameters for thin nanoabsorbers by the two-resonator method using TE and TM modes with maximums of electric or magnetic fields in the place of the sample. Table 5 presents results for nano-carbon and nano-ferrite absorbers ( $\epsilon_{par}$ ,  $\tan\delta_{\epsilon,par}$  have been extracted by the help of modes  $TE_{0mn}$  with  $m = 1, 2, 3$  and  $n = 1, 3$ ;  $\epsilon_{perp}$ ,  $\tan\delta_{\epsilon,perp}$  – modes  $TM_{0m0}$  with  $m = 1, 2, 3$ ;  $\mu_{par}$  – modes  $TM_{0mn}$  with  $m = 1, 2$  and  $n = 2$ ;  $\mu_{perp}$  – modes  $TE_{0mn}$  with  $m = 1, 2, 3$  and  $n = 2, 4$ ). Dielectric parameters of carbon-content absorbers strongly depend on the frequency, which corresponds with the results from other methods (§5.4).

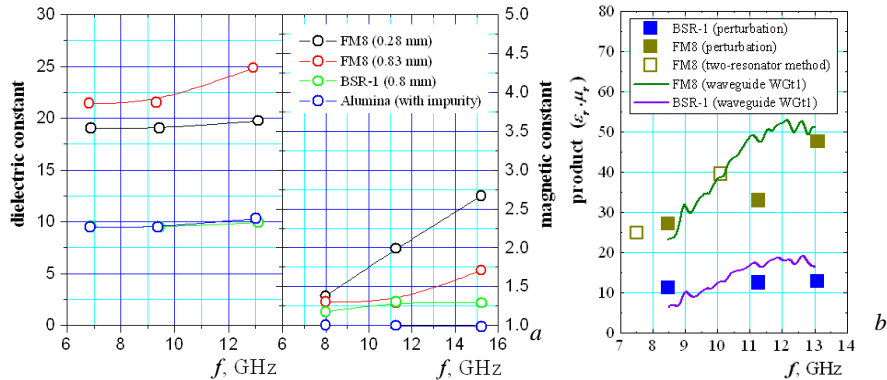


**Fig. 2.15.** a) Measured dielectric and magnetic constants of two commercial absorbers by perturbation method; b) measured product  $\epsilon_r \times \mu_r$  by three different methods

**Table 5.** Extracted values of the dielectric and magnetic parameters of 30- $\mu\text{m}$  thick nano absorbers (AUT) mixed with protective lacquer L (nC – consists of nano-carbon particles of diameter  $\sim 3\text{-}4$  nm; nF – nano-ferrite  $\text{Fe}_3\text{O}_4$  particles of diameter  $\sim 20\text{-}30$  nm; nFnC – a mixture nF : nC = 1 : 1)

AUT + L	$\epsilon_{par}/\tan\delta_{\epsilon,par}$ (f, GHz)	$\epsilon_{perp}/\tan\delta_{\epsilon,perp}$ (f, GHz)	$\mu_{par}$ (f, GHz)	$\mu_{perp}$ (f, GHz)
nC	7.65/1.6 (12.8); 6.82/5.4 (22.1); 3.49/5.5 (32)	4.20/0.22 (7.6); 4.04/0.15 (17.5); 3.56/0.22 (27.4)	-	-
nF	3.75/0.58 (12.8); 3.73/4.1 (22.1); 4.17/1.70 (32)	2.05/1.93 (7.6); 2.54/0.55 (17.5); 2.24/0.26 (27.4)	1.06 (20.8)	0.93 (15.7); 0.51 (24.4); 0.45 (33.8)
nFnC	8.84/3.3 (12.8); 5.82/0.25 (22.1); 2.51/0.77 (32)	2.57/0.73 (7.6); 2.67/0.08 (17.5); 2.62/0.144 (27.4)	1.16 (20.8)	1.04 (15.7); 1.50 (24.4); 2.90 (33.8)

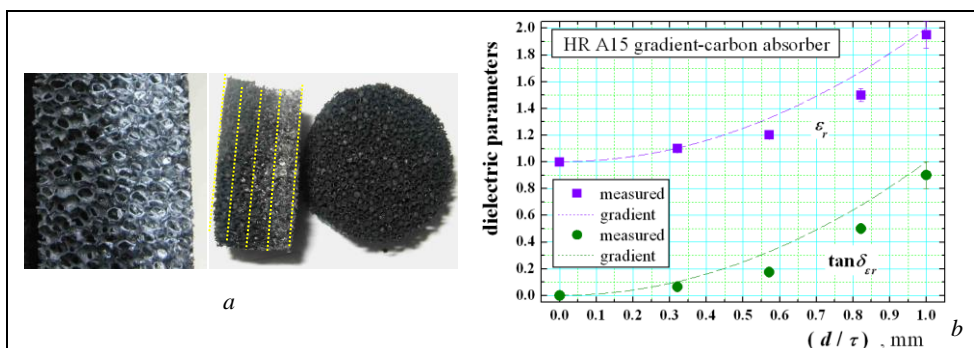


**Fig. 2.16.** *a)* Carbon-gradient sample ECCOSORB® HR A15; *b)* dependencies of the dielectric constant and dielectric loss tangent of four disk slices from 14-mm thick absorber

The last example is connected with the characterization of an innovative type of foamed absorbers with gradient carbon distribution – see illustrations in Fig. 2.16*a*. We performed relatively thin slices from the thick materials  $\tau \sim 14$  mm and managed to confirm this distribution as for the dielectric constant  $\epsilon_r(d) = 1 + (d/\tau)^2$ , as well as for the dielectric loss tangent  $\tan \delta_{\epsilon_r}(d) = 0 + (d/\tau)^2$  (dependencies in Fig. 2.16*b*). Such absorbers have decreased reflectivity; we proposed in [A52] this material to be used for decreasing of the radar cross-section of unmanned vehicles.

### 3. DIELECTRIC PROPERTIES AND ANISOTROPY OF CRYSTALLINE MATERIALS

As we mentioned in [1] (§2.3), the crystalline anisotropy of single- or polycrystalline materials (glasses, ceramics, artificial soft and low-temperature co-fired ceramics LTCC, liquid crystals, ferrites, semiconductors, etc.) is one of the oldest known types of well-expressed material anisotropy. Typically, these materials are homogeneous, but the anisotropy appears due to the existence of different crystallographic axes in their lattices and the fact that charges oscillate by different manner along to these directions. Our first investigations were connected exactly with this type of anisotropy of ceramic, ferrite and semiconductor disks, cylinders, rings and rods by different microwave methods [A3-A5, A7]. Then we continued with the characterization of crystalline and crystalline-like materials by the two-resonator method [A24, A35, A55, A58] and applying combinations with other broadband methods [A61, A62]. Here we will present short summarized information for these difficult for characterization materials.

#### 3.1. CRYSTALS, CERAMICS, GLASSES, SEMICONDUCTORS

The determination of dielectric properties of single or poly-crystalline materials is a classical problem in the microwave frequency range [19]. There exist different methods for characterization of the dielectric properties of crystals; the most accurate are the resonance ones [20]. However, an additional

circumstance for these materials is the presence of relatively strong bi-axial anisotropy (considered in [1], §2.3) – different dielectric parameters along the different axes, e.g.  $\epsilon_{xx} \neq \epsilon_{yy} \neq \epsilon_{zz}$  and  $\tan\delta_{\epsilon_{xx}} \neq \tan\delta_{\epsilon_{yy}} \neq \tan\delta_{\epsilon_{zz}}$ . In two our papers [A55, A58] we especially applied two-resonator method for characterization of high-Dk materials like ceramics, glasses, ferrites, semiconductors, etc. These papers aimed to show the ability of this resonance method to determine the crystalline anisotropy with acceptable accuracy and how this information can be used for crystalline sample characterization.

Table 6 (part 1) presents dielectric parameters and calculated anisotropy of different ceramics, performed as disk samples, which fit the measurement resonators' diameters. They are low-loss and relatively high-Dk materials, suitable

**Table 6.** [A58] (Part 1) Dielectric parameters and uni-axial anisotropy of ceramic samples, measured by two-resonator method (R1 &R2); (Part 2) Dielectric parameters and anisotropy of three disk samples measured by TE-mode resonator R1 in position D1 and D3(resonator axis lies along to 0z)

No	Sample; reference values Part 1			Anisotropy $\Delta A_g / \Delta A_{\tan\delta_g} \%$
		$\epsilon_{par} / \tan\delta_{\epsilon_{par}}$	$\epsilon_{perp} / \tan\delta_{\epsilon_{perp}}$	
1	Alumina (Al <sub>2</sub> O <sub>3</sub> ) 9.8-10.7	9.65/0.0003	10.35/0.0004	-7.0/-29
2	Polycore (Al <sub>2</sub> O <sub>3</sub> + 0.3% MgO)	10.044/0.0002	9.21/ 0.0003	8.7/-40
3	Sitall (glass ceramic)	8.19/0.0042	7.16/ 0.0038	13.4/10
4	3M @Epsilon 10 9.8/0.0020	11.64/0.0022	9.25/0.0045	22.9/-69
5	Rogers @TMM10i 9.9/0.0020	11.04/0.0019	10.35/0.0035	6.5/-59
6	Rogers @Ro3010 10.2/0.0035	11.74/0.0025	10.13/0.0038	14.7/-41
7	RT Duroid@ 6010 10.2/0.0023	10.71	10.252	4.4
8	ACX@ LTCC 7.5/0.003	7.60/0.007	6.68/0.0075	12.9/-6.9
9	YIG Garnet 14.8; Ms 1.7 kA/cm	15.83/0.00020	13.11/0.00027	18.8/-30
Part 2				
				
1a	Alumina (Al <sub>2</sub> O <sub>3</sub> ) 9.8-10.7	9.78 / 0.00080	10.20 / 0.00075	-4.2/6.5
8a	ACX@ LTCC 7.5/0.003	7.66 / 0.0069	6.20 / 0.0048	21/36
10	MgTiO <sub>3</sub>	14.61 / 0.00028	15.10 / 0.00018	-3.3/44

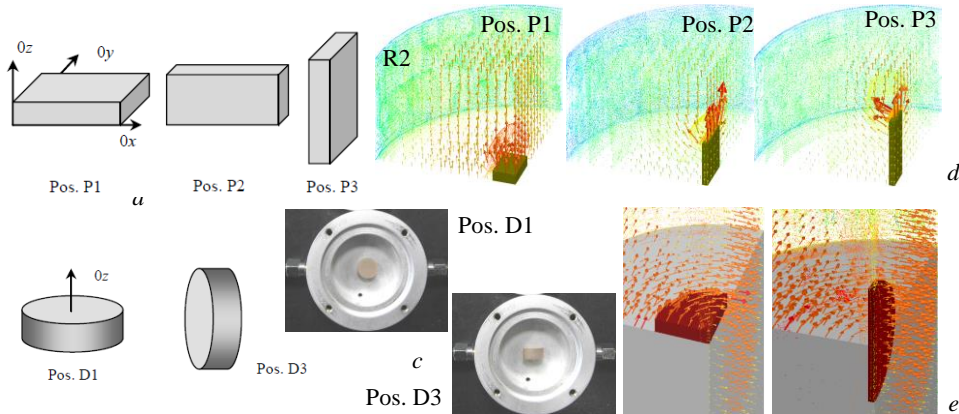


**Fig. 3.1.** Possible sample position in resonators for: prisms (a), disks (b); c) photo of samples in TM-mode resonator R2 in positions D1 and D3; d, e) illustration of the E-field vector distribution in the measurement resonators R2 (TM<sub>010</sub> mode) and R1 (TE<sub>011</sub> mode)

**Table 7.** Dielectric constants and anisotropy of several prismatic samples measured by TM-mode resonator R2 in positions P1, P2 and P3 (resonator axis lies along to Oz)

No	Sample description	 $\epsilon_{xx}$	 $\epsilon_{yy}$	 $\epsilon_{zz}$	$A_{\epsilon_{zz}}, \%$	$A_{\epsilon_{xy}}, \%$
1	Quartz (single crystal, c-axis =Oz)	3.74	3.84	4.27	-13.2	-10.6
2	Quartz (fused)	4.32	4.31	4.325	-0.12	-0.35
3	Silica glass	5.15	5.23	4.30	18.0	19.5
4	Mica (multi-layer silicate)	4.87	4.70	3.00	47	44
5	Optical glass LiNbO <sub>3</sub>	32.25	29.3	22.8	34	25
6	Crystalline Si for wafer	10.75	10.15	8.125	28	22
7	Semi-isolated GaAs wafer	11.30	11.10	7.90	36	34

for compact microwave integrated circuits MIC's, but the relatively big difference between the absolute values of parallel and perpendicular dielectric constants is indeed a serious design problem. Usually  $\epsilon_{par} > \epsilon_{perp}$ ;  $\Delta A_{\epsilon} \sim 9\text{-}15\%$  (only for the popular polycrystalline Alumina substrate we measure  $\epsilon_{par} < \epsilon_{perp}$ ;  $\Delta A_{\epsilon} \sim 7\%$ ). The attractive artificial soft ceramics (3M®Epsilam10, Rogers® Ro3010, TMM 10i), plastic substrates with high-Dk filling, show even bigger anisotropy (7-23 %), excluding the relatively isotropic RT Duroid®6010,  $\Delta A_{\epsilon} \sim 4.4\%$ ). The new class of low-temperature co-fired ceramics LTCC, applicable in the monolithic MIC's and promising for the mm-wavelength range, also have noticeable anisotropy ( $\Delta A_{\epsilon} \sim 13\%$ ). In general, our results for high-Dk ceramics are accurate, but difficult to be obtained – disk samples with fixed diameters should be prepared.

That's why, we proposed in [A55,A58] another variant of the two-resonator method for easier anisotropy determination: to use separately either TE- or TM-mode resonators (R1 or R2; [1] §3.2), but now for smaller disk or prismatic samples with different orientations parallel or perpendicular to the E fields – see the illustrations in Fig. 3.1a,b,c. However, the analytical model of the measurement resonators, described in [A22, A27] cannot be used; suitable 3D models for numerical simulations have to be applied now (examples have been given in Fig. 3.1d,e). Table 6 (part 2) presents again the dielectric parameters and anisotropy of some of the disk samples in part 1, but now measured by TE-mode resonator R1 in positions D1 and D3 – the coincidence is good. The variant with prismatic samples allows us to determine the actual bi-anisotropic parameters of different high-Dk samples. Table 7 presents the measured values  $\epsilon_{xx}$ ,  $\epsilon_{yy}$ , and  $\epsilon_{zz}$  in positions P3, P2 and P1 of several glasses and semiconductor wafers and the corresponding anisotropy  $\Delta A_{\epsilon_{x,y}}$ . The new information from these data is the expected fact that the single crystals show bigger anisotropy than the anisotropy of the corresponding poly-crystalline sample. For example, fused and single-crystal Quartz samples have equal values for the perpendicular permittivity,  $\epsilon_{zz} \sim 4.27\text{-}4.32$  (the *c*-axis coincides with the resonator axis Oz), while the values for the parallel permittivity  $\epsilon_{xx}$ ,  $\epsilon_{yy}$  are different:  $\sim 3.74\text{-}3.84$  in the single crystal along the *a*-axes;  $\sim 4.31\text{-}4.32$  in the fused Quartz. Relatively big anisotropy we observe for the crystalline Si and semi-isolated GaAs (last two rows in Table 7).

### 3.2. MICROWAVE FERRITES

The microwave ferrites, e.g. spinel, garnet, and hexaferrite systems as thin or thick films, powders, bulk samples, and nowadays different multiferroic materials, are key components in the systems that send, receive, and manipulate electromagnetic signals across very wide frequency range, from VHF up to mm-wave bands [21] and can ensure nonreciprocal behaviour. Microwave ferrites are very similar to the microwave ceramics (high dielectric constant  $\epsilon_f$  and low dielectric losses), but with this difference that they additionally possess magnetic properties – small magnetic constant ( $\mu_{dem} \leq 1$ ) and bigger magnetic losses, when no external dc magnetic field  $H_0$  has been applied (we will not consider the tensor magnetic properties in non-zero field  $H_0$ ). In our early papers [A4, A5, A7] we developed methods for determination of the dielectric constant  $\epsilon_f$  and saturation magnetization  $M_s$  of ferrite disks, prisms and cylinders, but calculated the demagnetized value  $\mu_{dem}$  by the known expression  $\mu_{dem} = (1/3)[1 + 2(1 - (\gamma M_s/f)^2)]^{0.5}$ , where  $\gamma = 3.5186$  MHz/(A/cm) is the gyro-magnetic ratio. Then in [A24], we began to measure the dielectric constant anisotropy of ferrites (Table 6, row 9). In our recent investigations of the Z-type hexaferrite  $\text{Sr}_3\text{Co}_2\text{Fe}_{24}\text{O}_{41}$  we managed to measure for the first time the full set of dielectric and magnetic parameters and the corresponding dielectric and magnetic anisotropy (for  $H_0 = 0$ ) above 3 GHz [A62]. In this case, we apply the following measurement procedure. The disk ferrite samples have been measured by the pair of resonators that support either  $\text{TE}_{0mn}$  modes (in R1) or  $\text{TM}_{0m0}$  modes (in R2) with samples placed in horizontal (1h) and vertical (1v) position in each resonator – see Fig. 3.2. The first several TE modes in R1 with  $m=1,2,3$  and odd  $n=1,3,5$  ensure extracting of parallel  $\epsilon_{par}$ ,  $\tan\delta_{\epsilon,par}$  (in 1h position) and perpendicular  $\epsilon_{perp}$ ,  $\tan\delta_{\epsilon,perp}$  (1v) die-

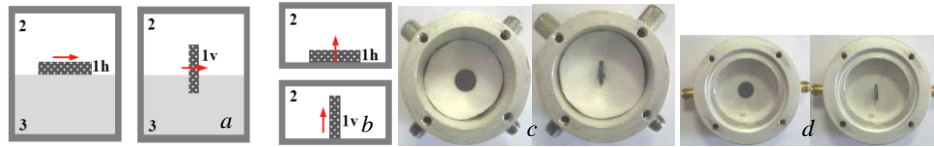


**Fig. 3.2.** Measurement resonators and sample position: a) Resonator R1 with  $\text{TE}_{0mn}$  modes ( $m = 1, 2, 3, n = 1, 2, 3, 4, 5, 6$ ); b) Resonator R2 with  $\text{TM}_{0m0}$  modes ( $m=1,2,3$ ); c, d) Photo of R1 and R2. Legend: 1h, 1v – samples in horizontal and vertical position; 2 – resonator; 3 – support foam

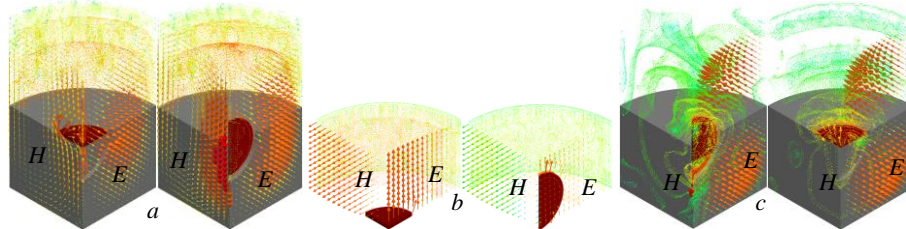


**Fig. 3.3.** E- and H-field distributions in resonators with samples in position 1h and 1v: a) R1 with  $\text{TE}_{011}$  mode; b) R2 with  $\text{TM}_{010}$  mode; c) R1 with  $\text{TE}_{012}$  mode

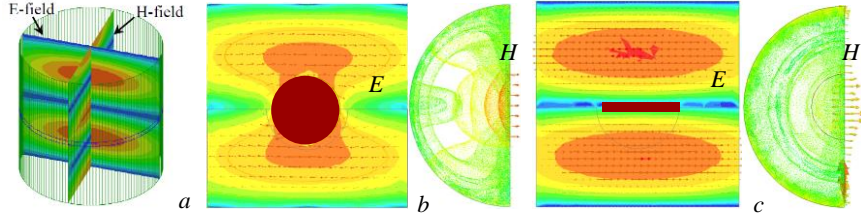


**Fig. 3.4.** E- and H-field distributions: *a)* R1 with TE<sub>112</sub> [A24]; *b)* R1 with TE<sub>012</sub> mode; sample in position 1v; *c)* R1 with TE<sub>012</sub> mode; sample in position 1h

**Table 8.** Extracted dielectric and magnetic parameters of hexaferrite Sr<sub>3</sub>Co<sub>2</sub>Fe<sub>24</sub>O<sub>41</sub> by the two-resonator method using different TE and TM modes for horizontally and vertically placed samples

Mode (resonance frequency, Q factor)	Sample orientation	Dielectric parameters: $\epsilon/\tan\delta_\epsilon$	Magnetic parameters: $\mu/\tan\delta_\mu$
TE <sub>011</sub> (12.4008/31.86)	hor.	<b>Par.: 15.02/0.076</b>	Perp.: 0.96/0.32
(13.0374/85.08)	vert.	<b>Perp.: 9.03/0.25</b>	Par.: 0.70/0.32
TM <sub>010</sub> (7.5620/31.86)	hor.	<b>Perp.: 9.92/0.445</b>	Par.: 0.70/0.30
(6.9632/194.5)	vert.	<b>Par.: 14.76/0.026</b>	Perp.: 0.96/0.32
TE <sub>012</sub> (15.6616/550.6)	hor.	Par.: 15.18/0.155	<b>Perp.: 0.92/0.70</b>
(15.6681/387.2)	vert.	Perp.: 7.95/0.47	<b>Par.: 0.70/0.32</b>
TE <sub>014</sub> (23.3829/963.1)	hor.	Par.: 14.20/0.070	<b>Perp.: 1.03/0.12</b>
(23.3907/511.0)	vert.	Perp.: 8.80/0.10	<b>Par.: 0.73/0.40</b>
<b>Averaged values (5-20 GHz)</b>		<b>Par.: 14.7/0.08   Perp.: 9.30/0.15</b> <b>Dielectric anisotropy: 45/-61 %</b>	<b>Par.: 0.75/0.20   Perp.: 0.98/0.10</b> <b>Magnetic anisotropy: -27/67 %</b>

lectric parameters because the sample falls in the E-field maximums (Fig.2.19a), while the first TM modes with  $m = 1, 2, 3$  – extracting of  $\epsilon_{perp}, \tan\delta_{\epsilon,perp}$  (1h) and  $\epsilon_{par}, \tan\delta_{\epsilon,par}$  (1v) (Fig. 3.3b). On the contrary, the first several TE modes with even  $n = 2, 4, 6$  in R1 has minimums of the E fields and maximums of H fields in the place of sample and allow us to extract with enough accuracy the magnetic parameters: in parallel direction  $\mu_{par}, \tan\delta_{\mu,par}$  (1v) and in perpendicular direction  $\mu_{perp}, \tan\delta_{\mu,perp}$  (1h) (Fig. 3.3c). In fact, only TE modes with even  $n$  index has pure H-field maximum and pure E-field minimums in the place of the sample (shown in Fig. 3.4; excluding very high samples, Fig. 3.4b); the TE modes with odd  $n$  index and TM modes have mixed E and H fields in the place of the sample (illustrated in Fig. 3.3a,b). These fields exist in mutually perpendicular directions: modes, which allow  $\epsilon_{par}$  extraction, have been influenced by  $\mu_{perp}$  and v.v. That's why the extraction procedure has been proposed as follows (the set of extracted values have been presented in Table 8). First of all, using TE modes with even  $n$  index and TM modes we determine intermediate values of the perpendicular and parallel dielectric parameters (Table 8: marked in grey) for  $\mu = 1$  and  $\tan\delta_\mu = 0$ . Using TE modes with odd  $n$  index we determine  $\mu_{par}, \tan\delta_{\mu,par}$  (1v) (for intermediate values  $\epsilon_{perp}, \tan\delta_{\epsilon,perp}$ ) and  $\mu_{perp}, \tan\delta_{\mu,perp}$  (1h) (for intermediate values  $\epsilon_{par}, \tan\delta_{\epsilon,par}$ ). Then, with the obtained intermediate magnetic parameters we extract the corresponding final dielectric parameters and finally, we apply the same procedure for the determination of corresponding final magnetic parame-

ters (Table 8: marked in black). Of course, there exists some inaccuracy for the obtained final  $\varepsilon$  and  $\mu$  parameters due to the differences between the resonance frequencies of the neighbour TE and TM modes. However, we apply additionally in [A62] a wideband method for final verifying of the frequency dependencies of ferrite material parameters (this procedure will be described later on). On the base of applied measurement methods we obtained the following averaged parameters for the considered Z-type hexaferrite  $\text{Sr}_3\text{Co}_2\text{Fe}_{24}\text{O}_{41}$  in the frequency range 5-15 GHz:  $\varepsilon_{par} \sim 14.7$ ;  $\tan\delta_{\varepsilon,par} \sim 0.08$ ;  $\varepsilon_{perp} \sim 9.3$ ;  $\tan\delta_{\varepsilon,perp} \sim 0.15$ ;  $\mu_{par} \sim 0.75$ ;  $\tan\delta_{\mu,par} \sim 0.20$ ;  $\mu_{perp} \sim 0.98$ ;  $\tan\delta_{\mu,perp} \sim 0.10$  (Table 8; last row). The measured anisotropy is relatively large, as for the dielectric parameters, as well as for the magnetic ones:  $\Delta A_{\varepsilon} \sim 45\%$ ;  $\Delta A_{\mu} \sim -27\%$ .

#### 4. PROPERTIES AND ANISOTROPY OF 3D PRINTED DIELECTRICS

The opportunity for 3D printing of different dielectric, metallic or mixed artificial materials provokes nowadays a lot of new applications of these materials in the microwave devices, including antennas. The 3D printing as a modern additive technology gives also the possibility to mix two or more dielectrics in one mixture with well-designed properties for microwave applications similar like the known reinforced substrates, textile fabrics, antenna radome composites, foams, absorbers, etc. Thus, the 3D printing is practically an ideal technology for producing of a variety of anisotropic metamaterials [22], but also isotropic or anisotropic filling materials with common purposes, e.g. foam-like and substrate integrated non-radiating dielectrics, and also metallized 3D printed devices.

##### 4.1. 3D PRINTED FOAM-LIKE ISOTROPIC DIELECTRICS

We began to investigate in [A49] the 3D printed structures regarding possible artificial anisotropy of the resultant materials, and established some preliminary conditions for obtaining artificial isotropy – see Fig. 4.1. The conclusion is that it is easier to produce anisotropic materials by 3D printing than artificially isotropic materials. For example, designers of Luneburg lens antennas by 3D printing [23] have to produce relatively big complex artificial

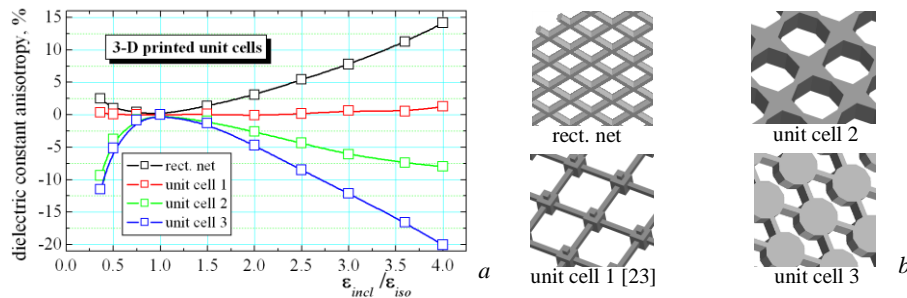


**Fig. 4.1.** Calculated dielectric anisotropy (a) of several 3D printed dielectrics with different unit cells (b) versus the ratio between the dielectric constants of inclusions and hosting substrate

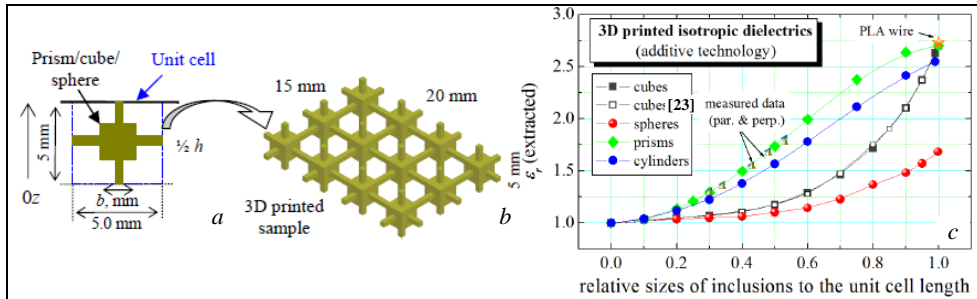


**Fig. 4.2.** Model of 3D printed sample: *a*) cubic unit cell 5×5 mm; *b*) whole substrate 15×20×5 mm; *c*) calculated and measured resultant dielectric constants by additive mixing technologies

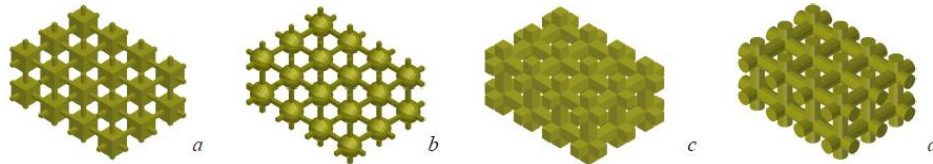


**Fig. 4.3.** Isotropic samples constructed by unit cells with: *a*) cube; *b*) sphere; *c*) prism; *d*) cylinder

dielectrics with a specific spatial distribution of the dielectric constant, but have to ensure also a practical isotropy/homogenization (Fig. 4.1, the unit cell 1). The main condition for obtaining of an isotropic distribution of the dielectric constant is the applying of fully symmetrical unit cells along to all three directions, which usually is in a contradiction with reliable mechanical properties of the whole printed body.

We discussed in our paper [A56] the possible 3D models, limitations and practical realization of artificial isotropic foam-like dielectrics by 3D printing, applying different suitable unit cells. The design strategy for the control of absolute values of the isotropic equivalent dielectric constant of these dielectrics has been demonstrated in Fig. 4.2 and Fig. 4.3. First of all, a suitable symmetrical unit cell can be selected with inclusions like cubes (Fig. 4.2a and [23]), spheres, prism, rhombs, cylinders or their combinations, supported by thin prismatic rods in all three directions. Then a bigger artificial substrate with appropriate dimensions has to be constructed by a repetition of the selected unit cell – Fig. 4.2b and Fig. 4.3. Finally, applying the procedure described in [1] (§2.4), we can calculate the equivalent (resultant) dielectric constant and loss tangent and compare with the measured values (Fig. 4.2c). The comparison for cube unit cell between our results and these in [23] is very good, at the comparison with measurement results for prism unit cell. This technology is very effective and accurate for construction of 3D printed homogenous dielectrics with the desired dielectric constant. It is ideal now for fast and accurate 3D printing on different lenses as antennas – [23, 24]. We developed 2009 in [A30] accurate step models for an approximation of the dielectric constant gradient distribution in Luneburg lens antennas and introduced effective 3D models for simulations of several variants of these promising antennas. Now we realize that these early models

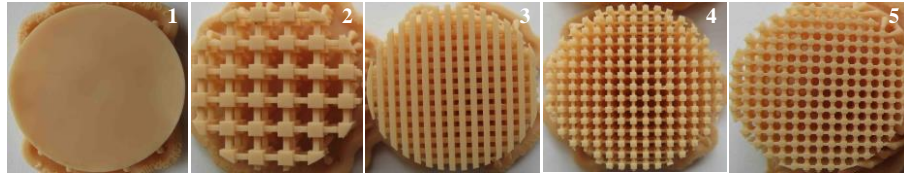


**Fig. 4.4.** 3D printed samples by Formlabs2® stereolithography (SLA) 3D printer applying dental model photopolymer resin FLDMBE01 (see the measurement results in Table 9)

**Table 9.** Measured dielectric parameters and anisotropy of 3D printed samples from Fig. 4.4

Sample description	thickness, mm	$\epsilon_{par}$	$\epsilon_{perp}$	Anisotropy $\Delta A_\epsilon$
1. Pure resin FLDMBE01	2.04	2.980	3.00	<b>-0.67</b>
2. Cubes 2x2 mm	7.70	1.332	1.330	<b>0.15</b>
3. Prisms 1x1 mm along to 0xy	9.30	1.497	1.450	3.19
4. Prisms 1x1 mm along to 0z	9.33	1.320	1.445	-9.04
5. Prisms 1x1 mm along to 0xyz	9.22	1.407	1.395	<b>0.86</b>

are fully applicable in the 3D printing of lens antennas and we have renewed our research on this topic. Fig. 4.4 presents several new 3D printed samples with controlled dielectric isotropy or anisotropy. They have been produced by Formlabs2 stereolithography (SLA) 3D printer applying photopolymer resin FLDMBE01, which ensures final accuracy  $\sim 25 \mu\text{m}$ . The measurements of the dielectric parameters of these samples by the two-resonator method allow us to prove the concept for the symmetrical unit cells and foam-like dielectric behaviour. Fig. 4.5 illustrates well this concept. We constructed basic 3D net with square prisms (side 1 mm) and added new prisms with different sides (2.5 and 4 mm) and tuned length, orientated in different directions. The result is an increase of the absolute anisotropy  $\Delta A_\epsilon$ , which depends on the degree of filling, nevertheless, if its sign is positive (for horizontal orientation) or negative (for perpendicular orientation of the prisms). Only for pure cubic unit cell, the anisotropy keeps its small absolute value (the research is still in progress [A66]).

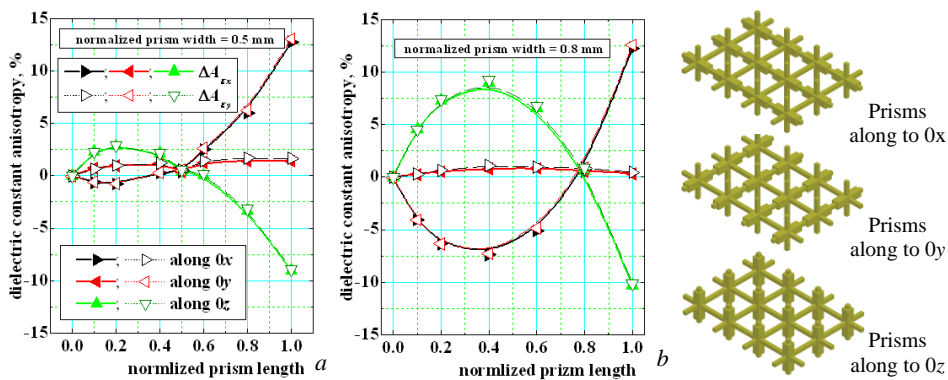


**Fig. 4.5.** Dielectric constant anisotropy of 3D printed nets with prisms with different sides and lengths (both normalized to the unit cell length 5 mm)

#### 4.2. 3D PRINTED DIELECTRICS WITH NON-SYMMETRICAL UNIT CELLS

The 3D printers generally save time and material by making the interior of the printed object not completely solid (with low infill density). The hexagonal and rectilinear (grid) infill are the most common because the samples are strength and light. However, due to the poor symmetry, the resultant anisotropy of samples with hexagon infill is relatively big for electrodynamic purposes. Fig. 4.6a presents the dependence of uni-axial anisotropy  $\Delta A_\varepsilon$  on the outer hexagon side length  $a$  (normalized to the whole sample height  $h$ ). The sign is negative for the chosen absolute height  $h=2$  mm; an absolute maximum appears, when the cell length is close to the height, i.e.  $a \sim h$ . In the case of mixed hexagonal-triangle filling, this maximum has been shifted for higher  $a/h$ . The anisotropy depends also on the width  $w$  of the hexagonal walls – see Fig. 4.6b; there also exists an absolute maximum for  $\Delta A_\varepsilon$  (the sign is negative for the fixed height). However, the most interesting is the  $\Delta A_\varepsilon$  dependence on the sample height  $h$  – see the corresponding curve in Fig. 4.6b for the normalized height to the hexagon length  $a$ . We can clearly see that the anisotropy can have as positive, as well as a negative sign. In our case, when the height  $h$  is about 20 % from the cell length  $a$ , the anisotropy is  $\Delta A_\varepsilon \sim 0$ . This is an important fact – the equivalent dielectric constant of 3D printed dielectrics depends on the sample height! It shows also how difficult is to achieve isotropy of such materials on the base of hexagonal (or other non-symmetrical) filling.

We managed experimentally to prove this effect. Table 10 presents the measured dielectric parameters and anisotropy of several home-made samples from polylactic acid (PLA) polymer, applying a very low-cost 3D printer.

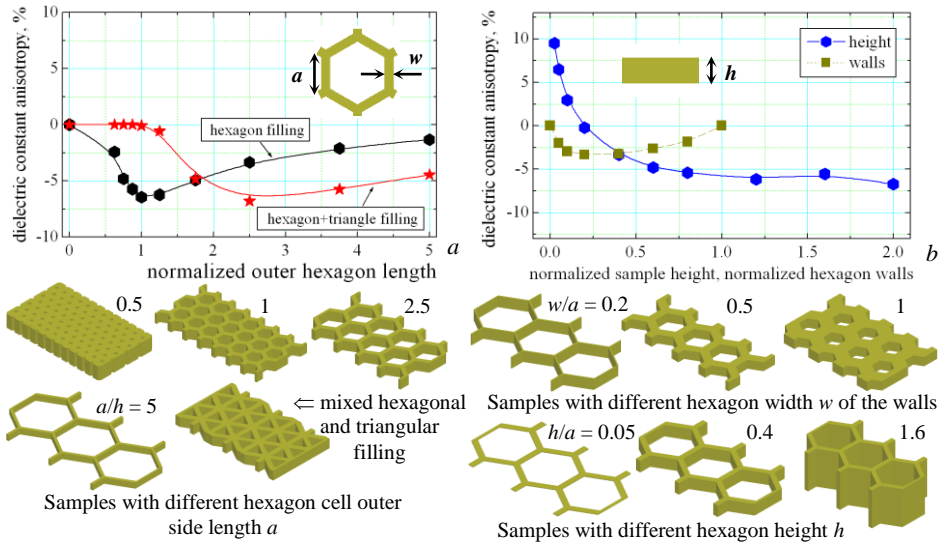


**Fig. 4.6.** Uniaxial anisotropy in 3D printed samples with hexagonal filling versus a) normalized outer side length  $a$  ( $a/h$ ); b) normalized hexagon width  $w$  and height  $h$  ( $w/a$ ;  $h/a$ )

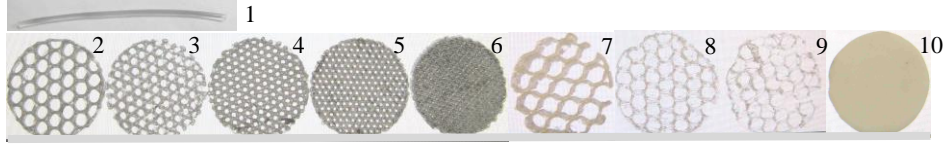


**Fig. 4.7.** 3D printed samples by fused deposition modelling with PLA filament applying low-cost 3D printer MakerGear®. Samples: pure PLA wire 1, samples 2-9 with infill 60-10 % and different height; dense (100 %) 3D printed photopolymer 10 (see measurement results in Table 10)

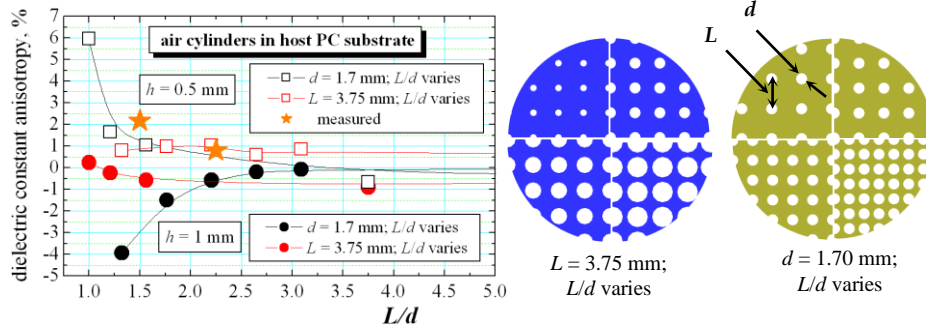
**Table 10.** Measured dielectric parameters and anisotropy of 3D printed samples from Fig. 4.7

Samples	$h$ , mm	$\epsilon_{par}/\tan\delta_{\epsilon,par}$	$\epsilon_{perp}/\tan\delta_{\epsilon,perp}$	Anisotropy $\Delta A_{\epsilon}/A_{\tan\delta\epsilon}$ , %
1. PLA wire	$d = 2$	2.750/0.0080	2.750/0.0080	0/0
2. infill 20 %	1.85	1.310/0.00260	1.273/0.00146	2.9/56
3. 30 %	1.69	1.368/0.00287	1.328/0.00161	3.0/57
4. 40 %	1.88	1.555/0.00378	1.504/0.00229	3.3/49
5. 50 %	1.42	1.690/0.00493	1.620/0.00281	4.2/55
6. 60 %	1.68	1.810/0.00524	1.710/0.00310	5.7/178
7. 10 %	6.70	1.177/0.00158	1.216/0.00177	-3.3/-11.3
8. 10 %	1.30	1.111/0.00128	1.134/0.00093	-2.1/31
9. 10 %	0.96	1.035/0.00095	1.071/0.00052	-3.4/58
10. photopolymer 100 %	1.69	2.961/0.0049	2.960/0.0053	0.03/-7.8

The photos of some produced and measured samples have been given in Fig. 4.7. Nevertheless the non-perfectly produced samples, we can see the tendency: the anisotropy  $\Delta A_{\epsilon}$  increases with infill increase (3-6%; stronger for  $\Delta A_{\tan\delta\epsilon}$ ). A negative anisotropy has been observed for samples with predominant vertically deposited walls. A dense (~100%) 3D printed photopolymer sample shows well-expressed homogenization, which is an expectable fact. All these investigations are still in progress.

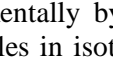
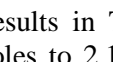
#### 4.3. ANISOTROPY OF SUBSTRATE INTEGRATED NONRADIATIVE DIELECTRICS

A new class of substrate integrated nonradiative dielectrics (SINRD) has been proposed in [25]. They are ordinary substrates with a drilled pattern of air holes. The idea is to decrease the equivalent dielectric constant and dielectric loss tangent and to increase the applicability of these artificial materials in the mm-wavelength range. A similar approach can be used also for easy construction of Luneburg lens antennas, made by slices with incorporated air holes [26]. However, in these cases, we again detect the already pointed reasons for appearing of uni-axial anisotropy – directed inclusions (air cylinders in this case), placed perpendicularly to the isotropic substrate surface. We performed special research on the influence of the incorporated air holes of diameter  $d$  at distance  $L$  on the dielectric constant and anisotropy of isotropic polycarbonate (PC) substrate. As in the case of 3D printed materials with non-symmetrical (e.g. hexagonal) filling, we found out that the dielectric anisotropy of SINRD strongly depends on the air inclusions' dimensions and substrate height  $h$  – see Fig. 4.8. The anisotropy  $\Delta A_{\epsilon}$  could be as with positive, as well as with negative sign for small  $L/d$  values.



**Fig. 4.8.** Dielectric constant anisotropy due to air cylinders in isotropic PC substrate (SINRD)

**Table 11.** Measured isotropic PC and anisotropic Arlon 25N samples without/with air via holes

Samples		<i>h</i> , mm	$\epsilon_{par}/\tan\delta_{\epsilon,par}$	$\epsilon_{perp}/\tan\delta_{\epsilon,perp}$	Anisotropy $\Delta A_{\epsilon}/A_{\tan\delta_{\epsilon}}\%$
Polycarbonate (PC)		0.50	2.765/0.0050	2.764/0.0049	0.04/2.02
PC + air holes ( <i>d</i> ~ 1.7)		0.50	2.474/0.00428	2.421/0.00409	2.17/4.54
Arlon 25N		0.513	3.645/0.00401	3.309/0.00287	9.67/33.14
Arlon 25N + air holes ( <i>d</i> ~ 1.5)		0.513	3.413/0.00365	3.113/0.00267	9.21/31.01

We tested experimentally by the two-resonator method the influence of perpendicular air via holes in isotropic PC sample and anisotropic commercial substrate Arlon 25N (results in Table 11). The anisotropy  $\Delta A_{\epsilon}$  increases for isotropic PC with air holes to 2.17 %, while the anisotropy in the anisotropic substrate slightly decreases due to the incorporated isotropic (air) inclusions.

#### 4.4. ANISOTROPY OF FRESH PLANT TISSUES WITH CELL STRUCTURE

The dielectric anisotropy of the fresh plant tissues with cell structure also can play an important role in the determination of the so-called fresh weight (FW). The nondestructive FW determination of young plant shoots, leaves, seeds, blossoms etc. is necessary for the diurnal regulation of plant growth and ensures valued information for the growing processes [27,28]. In [A50] we mana-

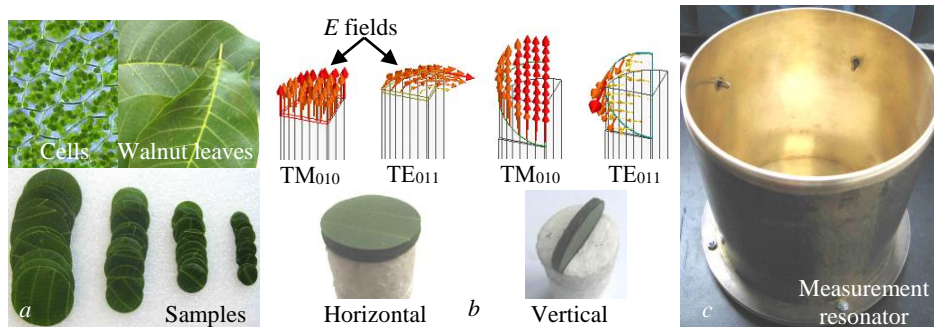


**Fig. 4.9.** a) Walnut leaves and disk samples under test; b) 3D models plant tissue of disk samples from leaves, placed horizontally and vertically on foam support in measurement cylinder resonator (c) with pair of  $TM_{010}$  and  $TE_{011}$  modes ( $D = 150$  mm,  $H = 172$  mm)

ged to show that the dielectric anisotropy of these tissues is very big as in fresh, as well as in a dry state, probably due to the specific hexagonal cell structure (as in the case of 3D printed samples). For the test we selected walnut leaves; we made disk samples and put them in vertical and horizontal positions in resonators (Fig. 4.9a,b), which support simultaneously TE<sub>011</sub> and TM<sub>010</sub> modes (Fig. 4.9c). Due to the different water content, the resonance shifts depends on the actual sample FW and can be used for building of a calibration curve “frequency shift  $\Delta f$ , MHz – fresh weight FW,mg” by staking together a different number of equal disk samples, increasing FW. However, we found out that the calibration curves differ for samples orientated vertically and horizontally; dependencies are given in Fig. 4.10. The reason definitely is the big leaves anisotropy. We determined the dielectric parameters of fresh and dry leaves – Table 12; both dielectric constants and anisotropy  $\Delta A_\epsilon$  decreases with the sample drying, remaining large – from 92 to 35 %. Thus, if we apply one of the obtained calibration curves for FW determination of plant with different leaves orientations (as in Fig.4.11 e), we will get wrong results. To prove our concept, we constructed 3D models of a fictive plant organism with three leaves (with stem) in different orientations, which have noticeable dielectric anisotropy (parallel/normal dielectric constant 35/5) – Fig. 4.11a-d. The obtained frequency shifts in MHz and recalculated relative FW are given in the insets. We can see that in both opposite cases (a, b) the shifts differ 19 times (!) for TM<sub>010</sub>. For leaves in an inclined position (c) or a mixed position (d) the shift is practically the mean value from both opposite

**Table 12.** Data for measured parallel and perpendicular dielectric parameters and anisotropy of samples from fresh and dry walnut leaves

Sample description	$\epsilon_{par}/\tan\delta_{\epsilon,par}$	$\epsilon_{perp}/\tan\delta_{\epsilon,perp}$	Anisotropy $\Delta A_\epsilon/A_{\tan\delta_\epsilon}\%$
Immediately after the pick-up of the leaves	24.8/0.315	9.15/0.235	92/29
1.5 hours after the pick-up of the leaves	16.1/0.305	7.65/0.225	71/30
Dry leaves	2.0/0.0525	1.4/0.0275	35/63

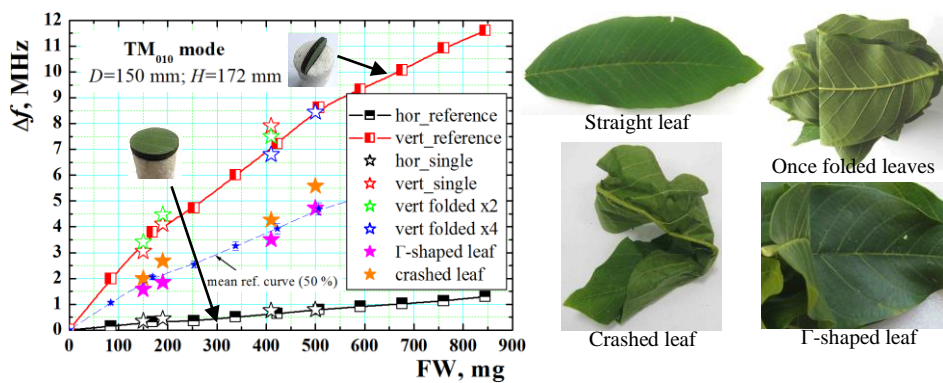


**Fig. 4.10.** Calibration curves for horizontal and vertical sample orientation: frequency shift v/s FW in mg for TM<sub>010</sub>-mode and positions on the plot for some unknown samples (single straight leaf, folded x 2/4, Γ-shaped or crashed walnut leaves)

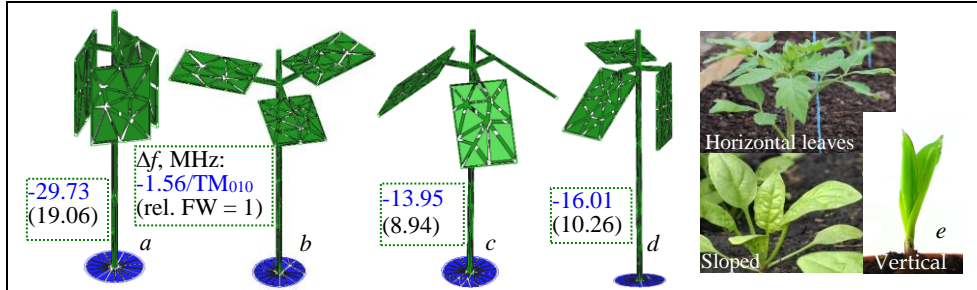


**Fig. 4.11.** 3D models of a fictive plant organism with 3 leaves placed: *a*) vertically to the resonator axis; *b*) horizontally; *c*) with slope 45 deg; *d*) mixed position (data in boxes: frequency shift and calculated FW relative to case *b*); *e*) examples for plants with different leaves orientation

shifts. For example, if we measure crashed or  $\Gamma$ -shaped (half of the leaf is placed vertically and the other half – horizontally) walnut leaves, the point for FW fall exactly in the middle zone between the pair of reference curves in Fig. 4.10. This fact gives a possible solution for the right prediction of the FW of the whole plant organism by nondestructive resonance method – to introduce a correction coefficient  $K$  depending on the predominant leaves' orientation in the real plant. Let the averaged relative portion of the horizontally placed leaves in the whole plant organism is  $x$  (determined by optical methods). If the frequency shifts for pure horizontal and pure vertical orientations of the plant leaves are  $\Delta f_h$  and  $\Delta f_v$ , the correction coefficient could be  $K = (1-x)\Delta f_v + x\Delta f_h$  and the actual fresh weight will be  $FW = K.FW_h$ , where  $FW_h$  is the fresh weight, which corresponds to pure horizontal orientation. For example, a mean reference curve is given in Fig. 7 for  $x = 0.5$  (50 %). Thus, for  $FW = 500$  mg of the  $\Gamma$ -shaped sample ( $x = 0.5$ ), the calculated coefficient is  $K \sim 4.61$  (the actual shift is 4.72, the measurement error is less than 2.4 %; instead  $\sim 600$  % without taking the anisotropy into account). Therefore, the correction procedure allows enough accurate determination of FW taking into account of the actual plant tissue anisotropy.

## 5. DIELECTRIC PROPERTIES AND ANISOTROPY OF MICROWAVE METAMATERIALS

The engineered microwave metamaterials and photonic band-gap crystals can be designed with controllable dielectric/magnetic constants along to the different directions. In this case, the artificial anisotropy is a fully desired property, which ensures unusual characteristics of some anisotropic metamaterial devices [29, 30] like invisibility cloaks, electromagnetic (EM) concentrators, EM-wave converters, etc. We will concentrate our attention on specific issues connected with experimental dielectric properties' characterization of these materials. As we already pointed in the first part ([1], §3), there exists a lot of measurement methods for material characterization, but only a few of them can determine with acceptable accuracy the artificial anisotropy. In this section, we will share our

experience for anisotropy characterization of metamaterials.

### 5.1. METAMATERIALS WITH METAL INCLUSIONS ON SUBSTRATE SURFACE

We began to present the results from our research on different types of metamaterials in [A49]. Then, in the paper [A53] we discussed the results of interesting research: two selected metamaterials as metal surface inclusions on a standard substrate have been measured by different methods and the extracted values of the equivalent dielectric constants have been compared. These materials have been developed for application in antenna radomes in the Ka-band. Fig. 5.1 presents the additional phase delay through samples' thickness, measured by a free-space method in the K/Ka-bands, and the extracted equivalent dielectric constant  $\epsilon_{eq}$  of samples, which photos have been given as insets. The first sample (“meta-disks”) exhibits behaviour as a standard dielectric with an increased dielectric constant in parallel directions (measured by the two-resonator method in [A49]). The second sample (“meta-surface”) placed horizontally, i.e.

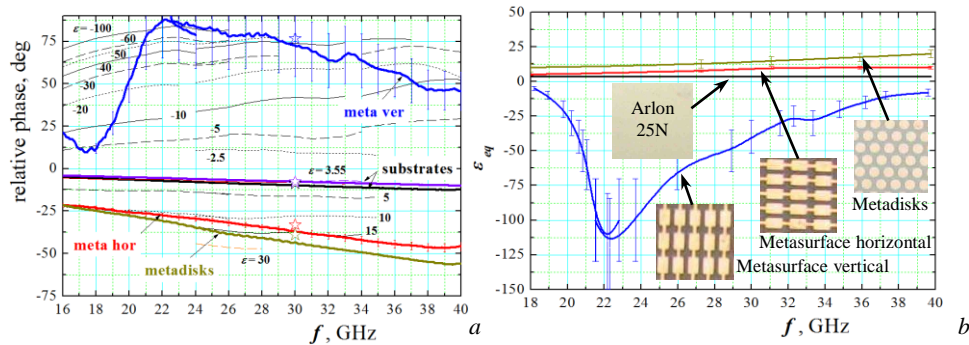


**Fig. 5.1.** *a*) Measured relative phase delay/advance by the free-space method in K/Ka bands through two types of metasamples with rectangular and disk metal inclusions (*sample 1* “meta-disks”: symmetrical planar unit cell with disks of diameter 3 mm and distance between them 4 mm, one-side printed on Arlon 25N (6 mils); *sample 2* “meta-surface”: non-symmetrical planar unit cell 3x1.5 mm two-side printed on substrate Arlon 25N (10 mils); *b*) extracted values of the equivalent dielectric constants of the samples; stars –simulated by HFSS® metasamples at 30 GHz

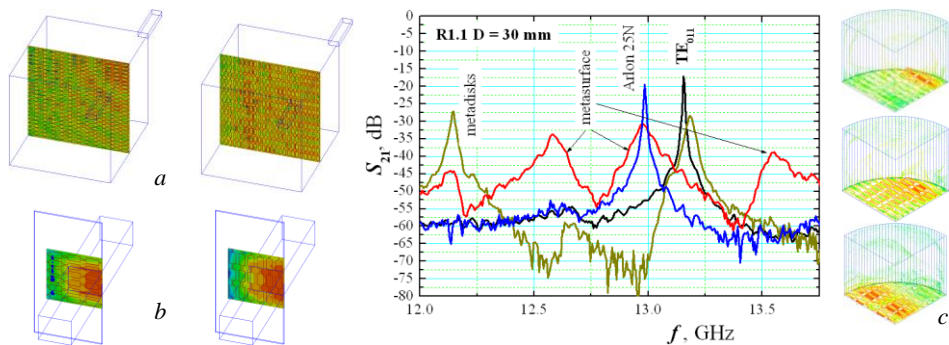


**Fig. 5.2.** Split 3D models for numerical  $\epsilon_{eq}$ -extraction by free-space method (*a*) and rectangular waveguide method (*b*). *c*) Measured excited  $TE_{011}$  mode in cylinder resonator with meta-samples (inset: calculated E-field distribution of parasitic resonances around the  $TE_{011}$  mode)

the rectangular unit cell is orientated perpendicularly to the electric field of the incident wave, shows similar behaviour of a dielectric. However, the same sample in vertical position causes opposite phase delay (phase advance; Fig. 5.1*a*) and the extracted parallel dielectric constant has a negative sign – Fig. 5.1*b*. The extraction has been performed by simulation of a specially constructed split 3D model of the metasamples – Fig. 5.2*a*. The considered samples remain the same dielectric behaviour by applying the rectangular waveguide measurement method – Fig. 5.2*b*, which is very popular for metamaterials (the extracted dielectric parameters have been presented in [A53]). However, the two-resonator method cannot be used for the characterization of metamaterials in all cases. Usually, the resonance measurements by TM mode resonators are normal, while the measurements by TE mode resonators sometime give multiple resonances instead one curve for a fixed mode. Fig. 5.2*c* illustrates this effect; due to resonance excitations in parts of the whole sample with metal inclusions a set of multiple resonance curves appears (as in measurements, as well as in simulations) and the right identification is impossible. In similar cases we cannot determine the metasample anisotropy for negative dielectric constants; the reasons have been explained in details in [A53, A61].

## 5.2. METAMATERIALS WITH CONTROLLABLE FILLING INCLUSIONS

In this section, we describe a successful attempt for the characterization of porous metamaterials using a combination of resonance and broadband methods [A60]. The objects of investigations are thin (6-100  $\mu\text{m}$ ) AAO layer from anodic  $\text{Al}_2\text{O}_3$  membranes with formed nano-scale air-filled pores. Such samples can be used as template matrices for incorporation into the pores of different nanostructured materials such as nanodots, nanowires and nanotubes with many nowadays applications [31, 32]. At this stage of our research, we are trying only to test the technology and the degree and type of inclusions are not well controlled. We prepared AAO samples with different relative purity (illustrated in Fig. 5.3; the purity depends on the degree of different technological contaminations). These initial investigations aim to determine for the first time in the microwave range their dielectric parameters and possible anisotropy and how the manufacturing technology influences these parameters. Table 13 presents the measured by the two-resonator method mean values of the parallel and perpendicular dielectric parameters for 4 selected samples with different purity. Definitely, samples with good purity (I, II) have a behaviour of the pure alumina ceramics with a set of air

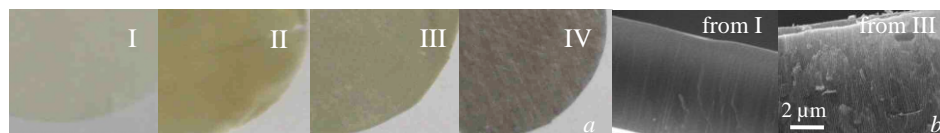


**Fig. 5.3.** *a*) View of anodic aluminium oxide (AAO) samples with decreasing purity (I, II – pure or relatively pure pores; III – pores with lossy magneto-dielectric contaminations; IV – pores with metal inclusions; *b*) microscopic side view of nanopores of diameter 35 nm

**Table 13.** Dielectric parameters and anisotropy of 4 typical disk AAO samples with different thickness (mean values for the frequency range 7-15 GHz) (more information in [A60]).

Samples	$D_s$ , mm, $h_s$ , $\mu\text{m}$	$\epsilon_{par}/\tan\delta_{\epsilon_{par}}$	$\epsilon_{perp}/\tan\delta_{\epsilon_{perp}}$	Anisotropy $\Delta A/A_{\tan\delta_{\epsilon}}$ , %
S0 (I)	29.7/42	5.96/-	9.68/-	-48/-
S1 (II)	26/30	5.00/0.011	9.95/0.0005	-66/183
S2 (III)	26/18	10.50/0.016	2.78/0.0175	116/-9
S3 (IV)	26/100	13.52/0.039	10.38/0.48	26/170

pores orientated in perpendicular directions: i.e.  $\epsilon_{par} < \epsilon_{perp} \sim 9.7-9.95$ . Thin samples with lossy inclusions (III) have opposite behaviour  $\epsilon_{par} > \epsilon_{perp} \sim 2.8$ , while both dielectric constants increase ( $\epsilon_{par}, \epsilon_{perp} > 10.4-13.5$ ) for samples, which include irregular metal contaminations. As we can conclude, in all cases the measured anisotropy is very big and this information can be used for fine technology adjustment of the porous AAO membranes.

However, such complex materials usually may have expressed frequency dependence of the dielectric parameters and anisotropy and even resonance behaviour. The applied here two-resonator method gives enough accurate information, but at fixed frequencies; to obtain informative dependencies in bigger frequency range we have to use another wideband transmission-line method (as the considered in [1], §3.4). Unfortunately, on this stage of technology, it is very difficult to print any metal layout on the considered AAO samples to form a measurable transmission line or resonator. Because of that, we applied another strategy for measurements – to obtain the needed information for the dielectric parameters, when the samples cover standard 50-Ohms planar lines: coplanar waveguide (CPW) or microstrip line (MSL) printed on a standard commercial substrate (in our case Arlon® 25N, 0.508-mm thick). We already applied this broadband method (Fig. 5.4) for a direct determination of equivalent dielectric constants of commercial substrates [A46], for metamaterials with metal surface inclusions [A53, A61], for thin nano-absorbers [A63], hexaferrites [A62] and Graphene-containing materials [A61].

In fact, the E fields of the dominant modes in both planar waveguides have mixed distribution (neither pure parallel nor pure perpendicular). The concrete proportions parallel-to-perpendicular E fields in the whole transmission lines

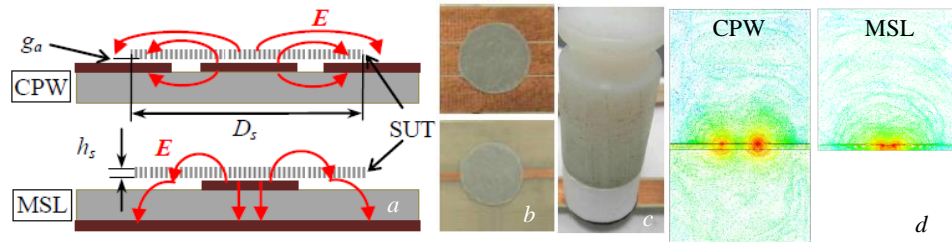


**Fig. 5.4.** a) Transmission-line method: cross-section view of coplanar waveguide (CPW) and microstrip line (MSL) covered by SUT ( $E$  – electric field patterns); b) SUT covers CPW and MSL; c) equal pressure has been ensured for all AAO samples; d) 3D models of CPW and MSL and  $E$ -field distribution (red colour – strong fields; green – medium fields; blue – weak fields)

(substrate and air space above) on 20-mils substrates have been estimated [A46] as  $\sim 38:62$  in MSL and  $\sim 79:21$  in CPW. Therefore, the covered CPW will extract predominantly value  $\epsilon_{eq}$  close to  $\epsilon_{par}$ , while the covered MSL – a mixed value  $\epsilon_{eq}$  between  $\epsilon_{par}$  and  $\epsilon_{perp}$ . We applied an extraction procedure for the determination of the equivalent dielectric constant  $\epsilon_{eq}$  (on the base of measured additional phase delay in CPW or MSL) and equivalent dielectric loss tangent  $\tan \delta_{\epsilon,eq}$  (only for lossy samples on the base of measured additional losses). This procedure has been developed applying simulations of well-constructed 3D models of the CPW or MSL structures (see Fig. 5.4d) with and without sample [A60]. Nevertheless, that the AAO samples have been placed on the CPW/MSL conductors under equal pressure (Fig. 5.4c), an unavoidable air gap  $g_a$  between the SUT and planar line conductors appears (Fig. 2.35a) due to different reasons: surface roughness, cleanness, curvature, etc. However, this gap can be accurately determined by a simple way: we can preliminary measure several isotropic materials with known dielectric parameters (e.g. PTFE;  $\epsilon_r \sim 2.05$ ; Polycarbonate,  $\epsilon_r \sim 2.78$ ; Kapton,  $\epsilon_{eq} \sim 3.16$ ). In the considered case the obtained effective air gap values are:  $g_a \sim 2.5 \pm 0.5 \mu\text{m}$  for MSL and  $g_a \sim 17.5 \pm 2.5 \mu\text{m}$  for CPW.

Fig. 5.5 gives the measured additional losses and phase delay in CPW/MSL

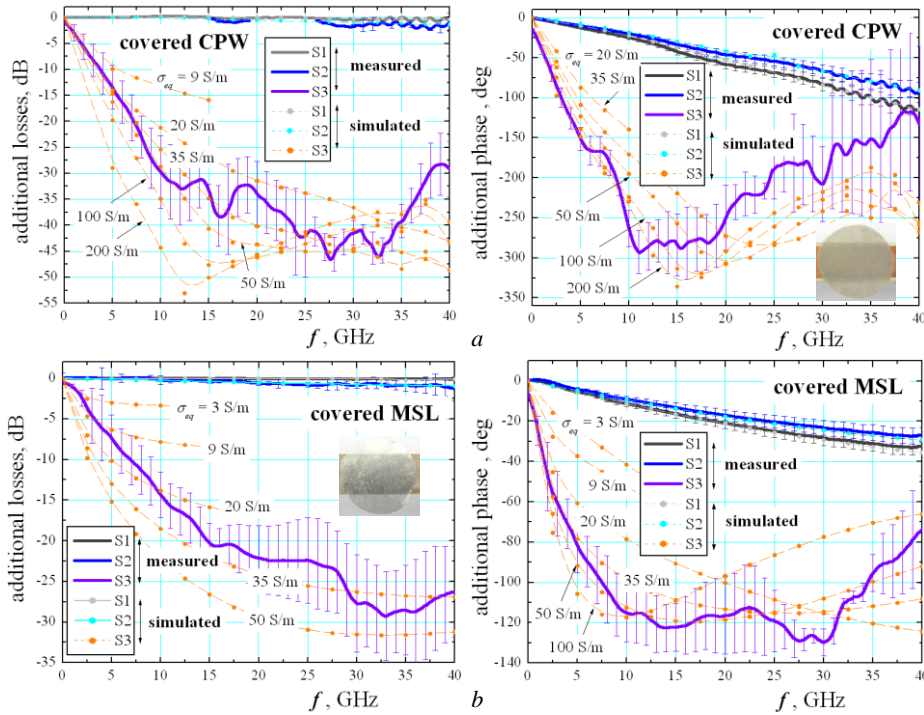


**Fig. 5.5.** Measured additional losses and phase delay in CPW (a) and MSL (b) transmission lines after covering by thicker AAO samples (solid curves). Theoretical dependencies (dashed curves), obtained by 3D simulations with dielectric parameters from Table 3 (anisotropy option) and setting of effective air gaps  $g_a = 2.5 \mu\text{m}$  (MSL) and  $17.5 \mu\text{m}$  (CPW)

transmission lines caused by the covering AAO sample. There are two ways to extract the dielectric parameters of AAO samples from these data: 1) to tune the equivalent parameters  $\epsilon_{eq}/\tan\delta_{\epsilon_{eq}}$  in the 3D models (Fig. 5.4d) until acceptable coincidence between the simulated and measured phase delay and losses (last for lossy materials only) has been reached or 2) to introduce in the 3D models the pairs of parameters  $\epsilon_{par}/\tan\delta_{\epsilon_{par}}$  and  $\epsilon_{perp}/\tan\delta_{\epsilon_{perp}}$  from the resonance measurements and to compare the simulated and measured dependencies. In this example, we selected the second way, taking the dielectric parameters from Table 13.

Samples S1,2 show behaviour as a pure dielectric (S1) or a relatively lossy dielectric (S2) – the additional losses are relatively small and the phase delay increases almost linearly with frequency increase; the practical coincidence shows that the dielectric parameters from the resonance measurements are fully correct. However, the sample S3 has behaviour as a conductive material. This type of behaviour has been expressed with a nonlinear phase delay, which can decrease at higher frequencies and observation of very big losses. If we neglect the conductivity, the calculated losses are few dB, considerably smaller than the measured (not shown). For that reason, we have to introduce additionally to the dielectric parameters for this sample also an equivalent conductivity  $\sigma_{eq}$ . During the simulations, we vary the  $\sigma_{eq}$  values and compare the theoretical and measured dependencies simultaneously for additional losses and phases. We can observe a strong  $\sigma_{eq}$  influence for both types of curves. The procedure for such a conductive sample is as follows. First, from the dependency for additional losses in MSL structure (Fig. 5.5b) we can evaluate the equivalent conductivity  $\sigma_{eq\_MSL}$  (the dielectric constant doesn't influence so much the losses). The obtained values are:  $\sigma_{eq\_MSL} \sim 3\text{-}10$  S/m (for the frequency range 1-5 GHz),  $\sim 10\text{-}20$  S/m (5-10 GHz),  $\sim 20\text{-}35$  S/m (10-30 GHz),  $\sim 35\text{-}50$  S/m (30-40 GHz). The simulated values for  $\sigma_{eq\_CPW}$  in CPW structure are similar (Fig. 5.5a); typically  $\sigma_{eq\_CPW} \sim 35$  S/m. Now, if we consider the phase delay dependence in MSL, the combination of values  $\epsilon_{eq\_MSL} \sim 9\text{-}10$  and  $\sigma_{eq\_MSL} \sim 35\text{-}40$  S/m is the solution for this conductive sample S3. The phase delay dependence in CPW gives slightly different combination,  $\epsilon_{eq\_CPW} \sim 11\text{-}12$  and  $\sigma_{eq\_CPW} \sim 50$  S/m; the difference means that the parallel dielectric constant and conductivity are bigger.

The obtained results for the dielectric characterization of AAO samples show that the proposed combination of resonance and broadband microwave methods is working well for such complex metasamples with variety of dielectric or metal inclusions. Samples with a small amount of metallic contamination can be better characterized with high accuracy. Samples with higher conductivity are also measurable: dielectric constants and anisotropy by the resonance method and equivalent conductivity – by the broad-band transmission-line method.

### 5.3. CARBON-CONTAINING MATERIALS

A good example of successful simultaneous determination of the pair of

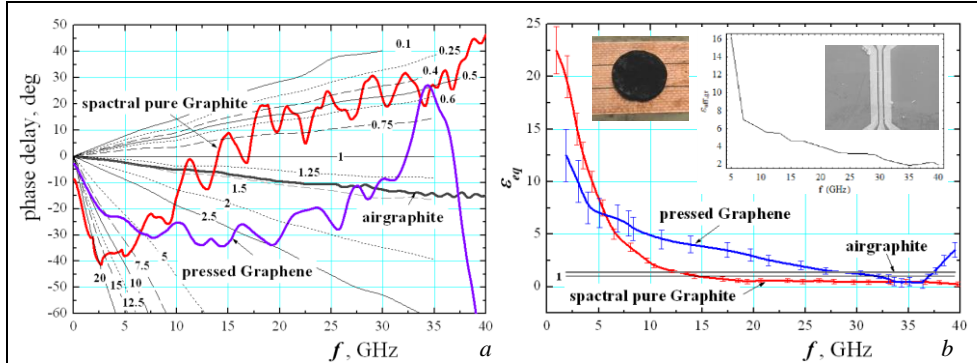


**Fig. 5.6.** *a*) Measured relative phase delay/advance in Graphite, air-filled Graphite and pressed Graphene samples by covered CPW (sample diameter  $\sim 9$  mm; thickness 0.9 mm;  $g_a = 20$   $\mu\text{m}$  gap “sample-conductor”; *b*) extracted  $\epsilon_{eq}$  values (inset: dielectric constant of graphene by [33])

equivalent parameters  $\epsilon_{eq}/\sigma_{eq}$  according to the Drude’s model for conductive dielectrics (when the loss tangent has been neglected; expression (6) in [1]) is the characterization of carbon-containing materials. In this section, we selected three types of samples: spectral pure Graphite, air-filled Graphite and pressed Graphene. The measured additional phase delay in CPW transmission line has been given in Fig. 5.6*a*, while the extracted equivalent dielectric constant  $\epsilon_{eq}$  – in Fig. 5.6*b* (when  $\sigma_{eq}$  has been neglected) [A53, A61]. The air-filled Graphite has a behaviour like a low-Dk dielectric;  $\epsilon_{eq} \sim 1.4$ -1.5). However, the other materials demonstrate completely different behaviour: the phase delay at lower frequencies transforms into phase advance (positive delay). In this case, the extracted  $\epsilon_{eq}$  values show strong frequency dependence – from 15-20 below 2 GHz up to 1 and even values below 1 for both Graphite and pressed Graphene samples. This dependence corresponds to the published results from other authors (e.g. [33]). However, the measured additional losses in CPW of these samples are very big (Fig. 5.7*a*) and cannot be explained with dielectric losses only; the samples have also a big equivalent conductivity  $\sigma_{eq}$ . As in the previous example, we can extract this parameter (the differences between samples are

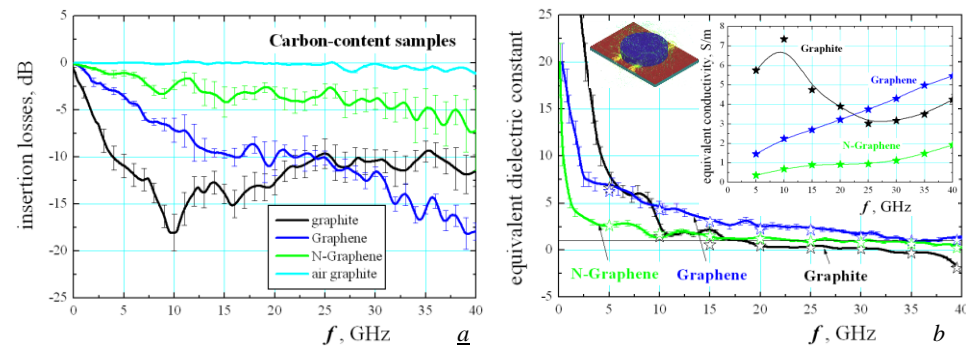


**Fig. 5.7.** *a*) Measured additional losses in CPW with carbon-content samples as an overlay; *b*) extracted frequency dependencies of  $\epsilon_{eq}$ ; stars: values of the equivalent dielectric constants by taking into account of the actual conductivity (inset: extracted equivalent conductivity  $\sigma_{eq}$ )

well observable; we added also the dependence for N-doped Graphene [34]). We established that the sensitivity and accuracy of the CPW measurement systems to the  $\sigma_{eq}$  changes are better in comparison to the MSL case; that's why we concentrate our efforts on CPW structure only. The extraction procedure now is as follows. We use in the 3D models (inset in Fig. 5.7b) the initial frequency-dependent  $\epsilon_{eq}$  values (determined for  $\sigma_{eq} = 0$ ; Fig. 5.6b) and starting to tune the conductivity to match the simulated and measured losses at a fixed frequency, we determine  $\sigma_{eq}$  at the same frequency. Then, simulating the phase delay/advance with the new  $\sigma_{eq}$  value at each selected frequency, we can recalculate the actual  $\epsilon_{eq}$  value – results for the extracted  $\epsilon_{eq}$  and  $\sigma_{eq}$  dependencies have been visible from Fig. 5.7b (the changes for  $\epsilon_{eq}$  are small). The measured  $\sigma_{eq}$  values in the frequency range 5-40 GHz are relatively small due to the air gaps in the samples.

#### 5.4. PLASMAS

Plasmas (gaseous, solid-state) are such media, which also can have an expressed anisotropy of their dielectric properties depending on the realized type of plasma discharge and orientation of the external magnetic fields (if exists). In our research, we developed several hairpin probes for resonance measurements of plasma densities in different directions [A28, A36, A38]. The hairpin probe is a simple quarter wavelength two-wire resonator, which can be relatively easy designed for TEM-mode operation [35, A28]. The open end of the structure ensures a maximum of the E field of the standing wave, which makes this resonance probe enough sensitive to the changes of the dielectric parameters of surrounding medium (e.g. effective plasma permittivity  $\epsilon_{p\_eff}$ ). The opposite short end has a maximum of the H field, which allows to achieve a quite stable and reliable magnetic coupling between the resonator and the feeding coaxial cable using H-type coaxial loop probe – see Fig. 5.8. The main benefit of this method in comparison with the other methods for plasma density evaluation is the fact that the measurements are based on a determination of the resonance frequency  $f_{hairpin}$  instead of any absolute measurements of E-field magnitudes, which ensure better sensitivity, accuracy and measurement simplicity.

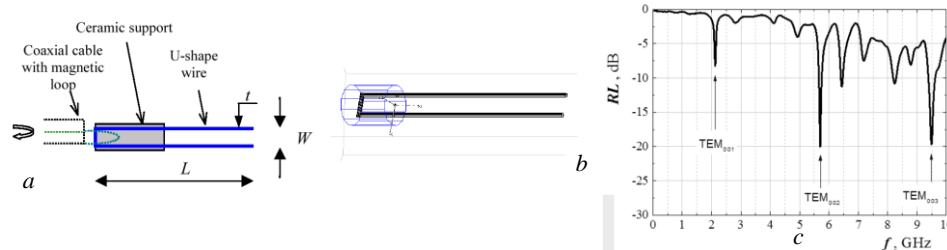


**Fig. 5.8.** a) U-shape straight (180-deg) hairpin probe and b) its 3D model in an eigenmode option of the simulator; c) measured return losses of the hairpin probe in the air with the exciting first three TEM-mode resonances (2-10 GHz)

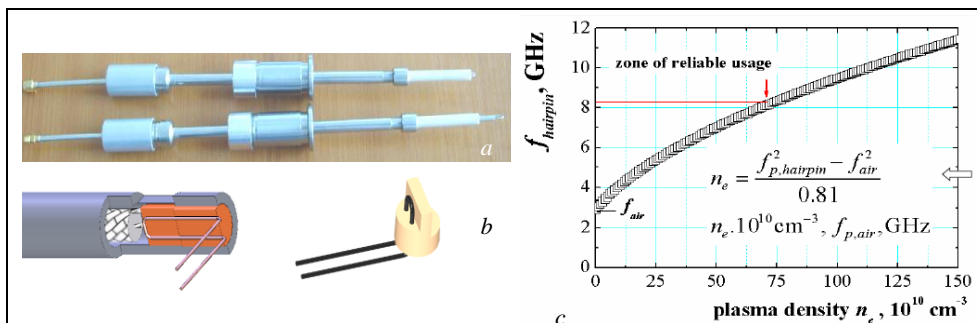


**Fig. 5.9.** a) Tools for mounting of the hairpin probe in the vacuumed plasma reactor; b) U-shaped hairpin probe orientated at 90 deg with ceramic support on the shorted end; c) dependence of the hairpin resonance frequency  $f_{hairpin}$  on the plasma density  $n_e$ . Inset: expression between  $f_{hairpin}$  and  $n_e$

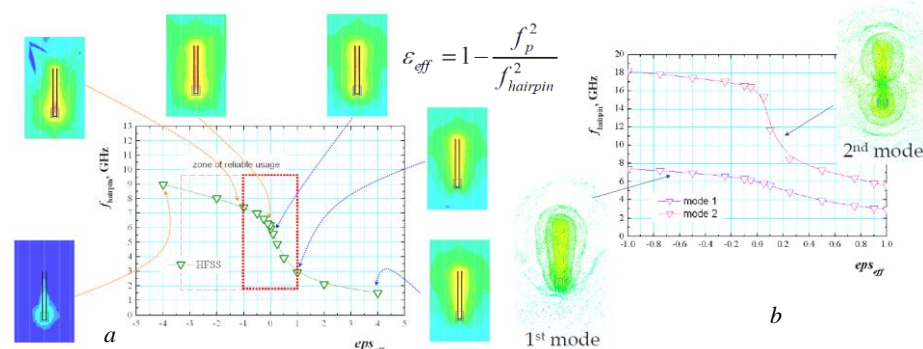


**Fig. 5.10.** a) Dependence of the hairpin resonance frequency  $f_{hairpin}$  on the effective plasma permittivity  $\epsilon_{eff}$  and simulated E-field distributions in different points. Inset: expression between  $\epsilon_{eff}$  and  $f_{hairpin}$ ; b) the same for the first two modes in the hairpin probe

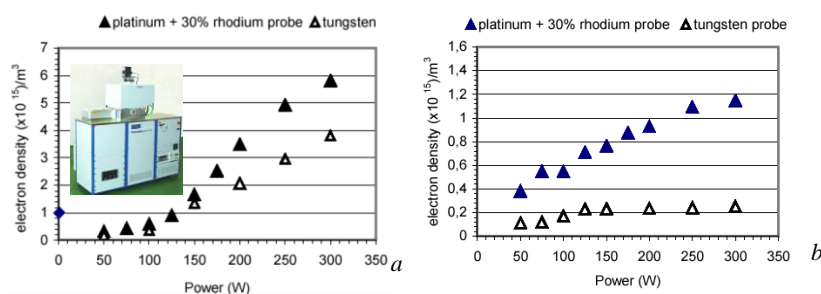


**Fig. 5.11.** Electron plasma density  $n_e$  v/s the reactor power (W) of 100-% oxygen plasma (a) and of 100-% SF<sub>6</sub> plasma at constant pressure (100 mTorr)

Fig. 5.9c illustrates the dependence of the hairpin resonance frequency  $f_{hairpin}$  on the electron plasma density  $n_e$  in a first-order approximation; similar dependence allows after calibration on air the relatively accurate determination of  $n_e$  during different plasma technological processes in vacuumed plasma reactors. The reason for existing of this dependence is the relation between the effective plasma permittivity  $\epsilon_{eff}$  and of the ratio between the plasma frequency  $f_p$

and the hairpin resonance frequency  $f_{hairpin}$  (see the inset in Fig. 5.10). In our research, we managed to determine the zone for reliable usage of this dependence (in the interval  $\varepsilon_{eff} \subseteq (1, -1)$ ; see Fig. 5.10a) between the area of saturation and the fact that the sensitivity of the hairpin probe increases by using of the high-order modes (Fig. 5.10b), if they have been well identified [A36].

We developed an experimental hairpin probe [A28] for implementation in plasma reactors with aggressive gases (as in [36]) like oxygen and SF<sub>6</sub>. The probes have been incorporated in some reactors of Oxford Instruments © (see [37]). The special features of this type of hairpin probes are: the used probe metal (Platinum + 30% Rhodium), which ensures bigger sensitivities than the conventional metals (see dependencies in Fig. 5.11) and a feeding coaxial cable filled with SiO<sub>2</sub>, which is working at relatively high temperatures in the considered plasma reactors.

#### 5.5. EXPERIMENTAL OBSERVATIONS OF ANISOTROPIC MAGNETO-DIELECTRIC EFFECTS IN A CLASS OF MULTIFERROIC MATERIALS

In [1] (section §2.3), we introduced the material properties of the so-called magneto-electric materials and the possibility for their characterization. These specific materials will play an increasing role as integrated tunable components in the modern microwave devices [38] due to the ability to separately control their magnetic properties by an external dc voltage and their electrical properties by an external magnetic field. However, the separation of these effects is not an easy fact. In our research we already managed to detect magneto-dielectric effects in several artificial materials in the frequency range 2-40 GHz [A61, A65, A68]. In this paper, we will briefly describe the experimental verification of magneto-dielectric effect in a multiferroic material Sr<sub>3</sub>Co<sub>2</sub>Fe<sub>24</sub>O<sub>41</sub> ([A62], see also §3.2).

In most cases, the magneto-dielectric effect in multiferroics has been measured at relatively low frequencies, (typically several hundred MHz, [39]). Only a few papers consider the characterization of this effect in the microwave range [40]. Here we describe an experimental characterization of dielectric/magnetic constants' variations of Z-type hexaferrite Sr<sub>3</sub>Co<sub>2</sub>Fe<sub>24</sub>O<sub>41</sub> in an external magnetic field. Fig. 5.12 illustrates the applied setup that combines measurements in the frequency range 0-40 GHz of CPW transmission line covered by magnetized sample by parallel or perpendicular external magnetic field  $H_0$  between 0 up to 2.4 kOe. The samples have been directly placed on the CPW conductor and the

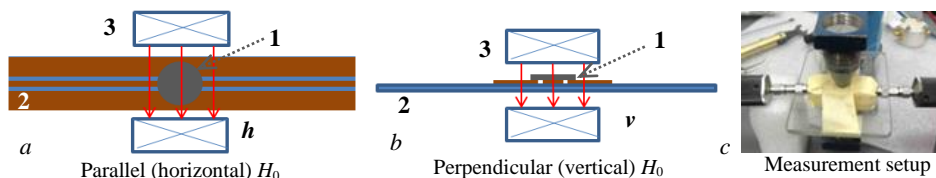


**Fig. 5.12.** Applied external dc magnetization of sample in parallel/horizontal (a) and in perpendicular/vertical (b) direction; (c) electromagnet system; Legend: 1 – sample; 2 CPW substrate; 3- electromagnet

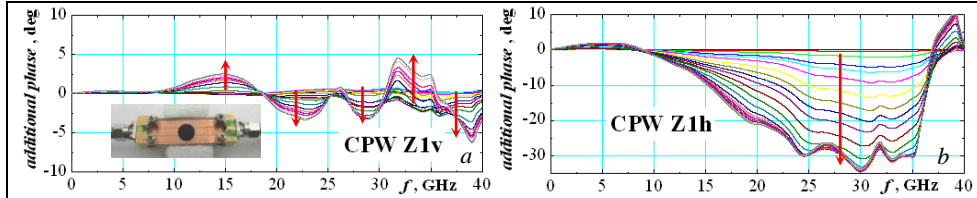


**Fig. 5.13.** Measured dependencies for the additional phase in CPW structure with multi-ferroic sample in vertical (*a*) and horizontal (*b*) magnetic field  $H_0 = 0$ -1.33 kOe, normalized to values at  $H_0 = 0$  (the red arrows show the directions for  $H_0$  increasing).

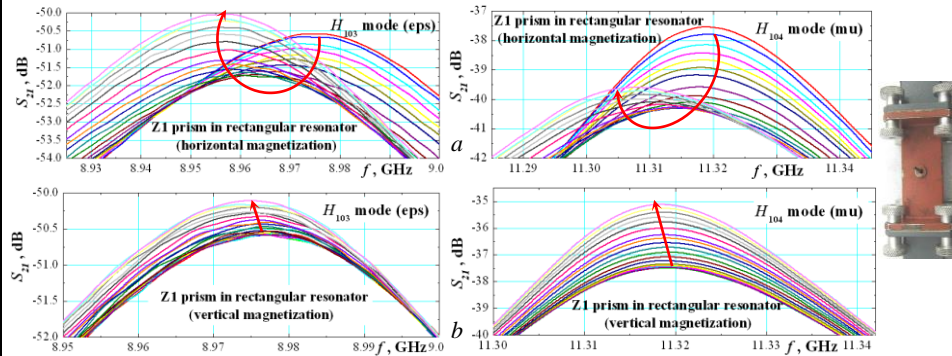


**Fig. 5.14.** Resonance curves of different modes in rectangular resonators (WR90) with prisms ( $1.22 \times 2.07 \times 10.16$ ) from multi-ferroic in the centre, which have been influenced only by the dielectric (eps) or magnetic (mu) constants of the sample in horizontal (*a*) and vertical (*b*) magnetic field  $H_0$  0-1.33 kOe (the red arrows show the directions for  $H_0$  increasing).

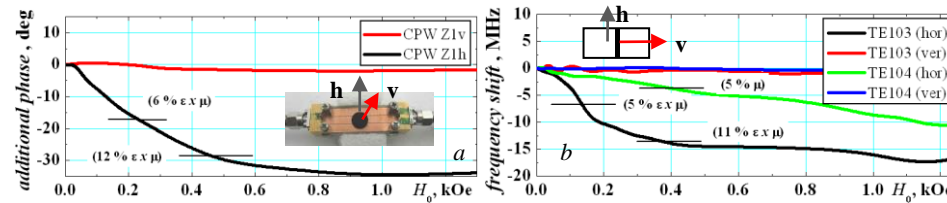


**Fig. 5.15.** *a*) Variations of the additional phase in CPW structure with multi-ferroic sample at 30 GHz v/s magnetic field  $H_0$ ; *b*) shift of resonance frequency of modes  $TE_{103}$  and  $TE_{104}$  due to magnetized multi-ferroic prism in magnetic field  $H_0 = 0$ -1.33 kOe, normalized to values at  $H_0 = 0$

additional losses and phases caused by the magnetized sample can be measured, when  $H_0$  increases. Fig. 5.13 *a, b* illustrates the differences in additional phase for  $H_0$  in both horizontal/vertical directions. The influence of the horizontal  $H_0$  is 5-6 times bigger, which clearly indicates anisotropy of the measured effect – Fig. 5.15*a*. However, we cannot separate in these measurements the dc magnetic field influence on the sample dielectric and magnetic constants. This information we can obtain by realized resonance perturbation measurements in a rectangular resonator with small ferrite prisms in the resonator center. From the changes in the resonance frequencies of the excited  $TE_{10p}$  modes (Fig. 5.14), we can separately extract the variation of the equivalent magnetic  $\mu_{eq}$  ( $p = 2, 4, 6$ ) and dielectric  $\epsilon_{eq}$  ( $p = 1, 3, 5$ ) constants of the ferroic sample. The analysis of the

results in Fig. 5.15b allows us to conclude that the smaller external magnetic fields ( $H_0 \leq 0.4$  kOe) influence stronger the dielectric constant  $\epsilon_{eq}$ , while the stronger fields ( $H_0 > 0.8$  kOe) – the magnetic constant  $\mu_{eq}$ , where  $\epsilon_{eq}$  variations show a saturation. These conclusions have been confirmed by the broadband CPW measurements; see dependencies in Fig. 5.15a, where a 10-12 % variation of the material constants can be achieved, which is enough for possible applications. The detailed investigations of the magneto-dielectric effects in ferroic and other types of materials are in progress [A66].

## 6. EQUIVALENT CONDUCTIVITY OF MATERIALS

Nowadays the conductivity of materials starts to play an increasing role in the design of new RF devices, comparable with the importance of the role of the actual dielectric and magnetic parameters in the same design. The microwave engineers need to know the actual equivalent conductivity of the metals and metallization layers used in different bulk and planar devices accurately to determine the conductor losses. Moreover, today many devices are realizing with metalized injection-moulded or 3D printed dielectrics instead solid metal walls, where the equivalent conductivity depends not only on the used metal but also on the surface roughness, cleanness, protective layers, etc. Many new materials in modern electronics have smaller than ordinary metals but noticeable conductivity – carbon-containing materials, metasurfaces, absorbers, conductive textile fabrics, etc. In this section, we present our experience in the area of characterization of equivalent conductivity in the interval from typical values for conductive metals (e.g.  $\sim 4-6 \cdot 10^7$  S/m) up to  $10^3-10^4$  S/m by resonance methods and up to 1-10 S/m by broadband methods.

### 6.1. EQUIVALENT CONDUCTIVITY OF METALIZED PLASTIC SAMPLES

The nowadays technologies for creating of innovative antenna components for airborne, satellite and different 5G applications – metalized plastic details, 3D printed structures, metamaterials with metal inserts, metalized composites or textiles, etc., sharply increased the needs to characterize the actual conductivity of these materials due to the purposes for more reliable 3D design. Actually, the determination of the conductivity  $\sigma_{MW}$  at microwave frequencies (instead of the widespread dc  $\sigma_{dc}$  or optical  $\sigma_{\infty}$  values) is a classical problem. It is a known fact also that the so-called effective conductivity diminishes for electroplated metal surfaces [41]. It depends not only on the skin depth but additionally on the surface cleanness, roughness, flatness, coatings, technological scratches and other surface irregularities. For this reason, we developed in [A43] an efficient microwave resonance method for determination of the useful parameter equivalent conductivity  $\sigma_{eq}$ , which better characterizes the metal surfaces in X-Ka bands and more or less differs from the dc bulk conductivity usually applied in the 3D simulators for antenna components' design. The idea of the method is

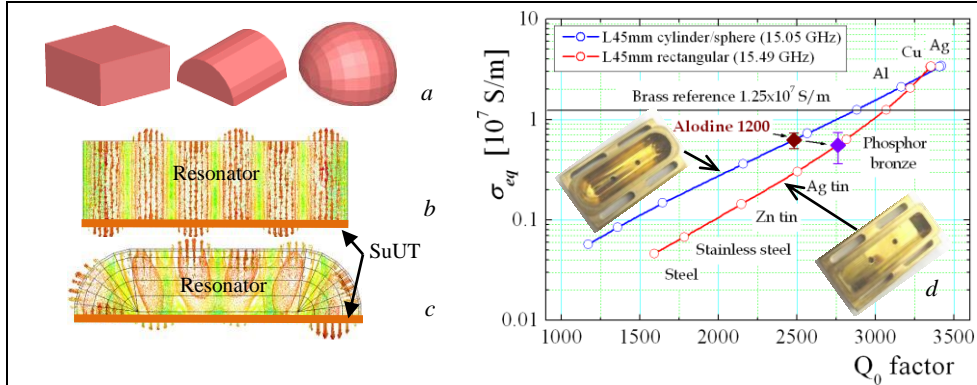


**Fig. 6.1.** *a)* Resonators with decreasing “volume-to-bottom surface” ratio; excited TE<sub>106</sub> mode in rectangular (*b*) and sphere-cylinder (*c*) measurement resonators; *d)* reference curves “ $\sigma_{eq} - Q_0$ ” with Brass reference for determination of equivalent conductivity of surface under test (SuUT)

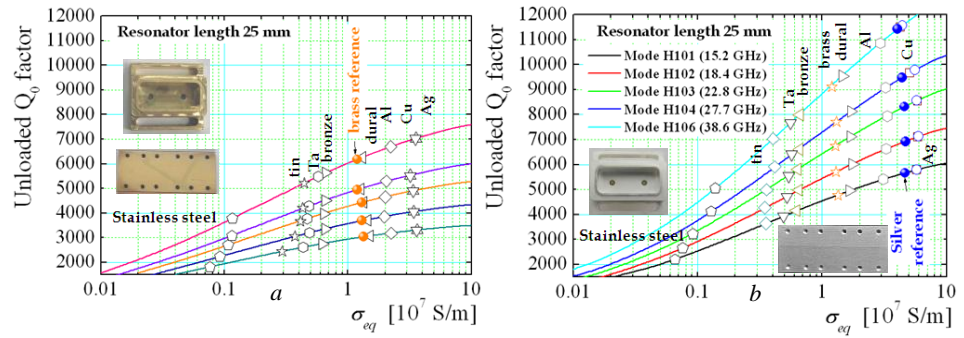


**Fig. 6.2.** Calibration curves “equivalent conductivity – unloaded Q factor” for the all-Brass resonator and “Brass conductivity reference” (*a*) and for the all-Silver resonator and “Silver conductivity reference” (*b*) and test values of conductivity for several conductive materials.

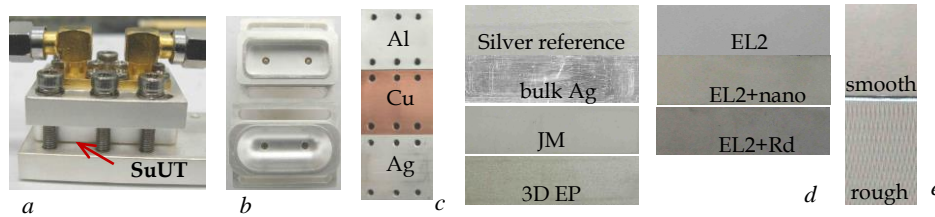


**Fig. 6.3.** *a)* Measurement resonator with SuUT; *b)* Two measurement resonators; *c)* Reference surfaces from Al, Cu and Ag; *d)* Surface of several samples: Reference Silver EP; bulk Ag; JM – sprayed Ag nano-coating; 3D EP – electro-plated Ag on 3D printed photopolymer; EL2 – electroless Ag; EL2+nano protective layer; EL2+Rd Rhodium protective layer; *e)* smooth and rough Al

based on the replacement of one flat surface of a selected volume resonator with the surface under test (SuUT). To increase the resonator sensitivity to the conductivity variation of SuUT, we started to search specific measurement resonators with small “volume-to-bottom surface” ratio (Fig. 6.1*a*). We selected two resonators – the standard rectangular resonator with excited TE<sub>10*p*</sub> modes (*p* = 1-6) (Fig. 6.1*b*) and a sphere-cylindrical resonator with excited similar modes

(Fig. 6.1c). Applying a “Brass reference” for calibration of the measurement systems, we managed to determine with satisfying accuracy the actual equivalent conductivity  $\sigma_{eq}$  of many metalized surfaces (e.g. Alodine 1200 passivation layers over Dural surfaces; Fig. 6.1d) used in different antennas. However, the benefit of using the sphere-cylinder measurement resonator could be minimized due to the complex E field distribution for higher modes and the “detachment” of that field from the bottom resonator wall (SuUT). Actually, the applying of a “Silver reference” for the measurement resonators can increase the Q factors of the excited modes twice and to additionally increase the sensitivity [A57]. The older calibration curve by the “Brass reference” covers the interval for accurate  $\sigma_{eq}$  determination from  $7 \cdot 10^7$  to  $5 \cdot 10^4$  S/m, while the new calibration curve by “Silver reference” covers considerable bigger interval – from  $7 \cdot 10^7$  up to 0.5 S/m – see the set of calibration curves in Fig. 6.2. The procedure for the determination of equivalent conductivity  $\sigma_{eq}$  of SuUT is as follows. First, the unloaded Q factors of all excited TE modes have to be measured in the resonator with silver-plated walls, including the “Silver-reference” as a bottom wall – Fig. 6.3a,b,c. The simulations of the 3D models for each mode (Fig. 6.1b,c) allow determining the equivalent conductivity of the resonator walls. Then the “Silver-reference” has to be replaced with the corresponding SuUT and the new unloaded Q factors to be measured. The new simulations by varying the conductivity only for the SuUT allow to achieve practical coincidence between the measured and simulated Q factors and to obtain the equivalent SuUT in the considered frequency range.

Applying this method, we managed to characterize the actual conductivity  $\sigma_{eq}$  of a lot of artificial metalized surfaces. First of all, we investigated the influence of the surface roughness, described by the parameter  $R_t$  – the total “peak-to-valley height” of the surface bulges. Fig. 6.3e shows two Dural surfaces: 1) “smooth” (with  $R_t < 0.05 \mu\text{m}$ ) and 2) “rough” (with  $R_t \sim 0.8\text{-}1.6 \mu\text{m}$ ). We established a decrease of  $\sigma_{eq}$  with  $\sim 10\%$  in Ku-band and  $\sim 25\%$  in Ka-band of rough surfaces compared with the smooth surfaces of the same sample [A43], which proves the acceptable sensitivity of the proposed measurement method.

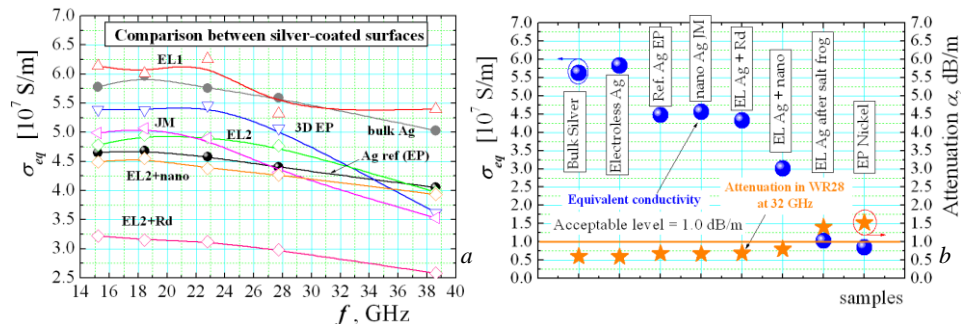


**Fig. 6.4.** a) Measured equivalent conductivity  $\sigma_{eq}$  of Ag-coated samples by different technologies (see the legend in Fig. 6.3d; all Ag layers are 5-12  $\mu\text{m}$  thick); b) Mean  $\sigma_{eq}$  (at 32 GHz) and calculated attenuation in WR28 waveguide for Ka-band for the considered samples

Fig. 6.3*d* illustrates the view of the top surfaces of several silver-coated plastic samples, prepared by different technology;  $\sigma_{eq}$  dependencies have been drawn in Fig. 6.4*a*. Acceptable values  $\sigma_{eq} = 4.6\text{-}6.2$  S/m are fully realizable by electro-less (EL), electro-plated (EP) or nano-Ag-aerosols-sprayed (JM [42]) technologies. The fine surface finishing (EL1) increases the conductivity with 15-20% (EL2); the protective layers decrease  $\sigma_{eq}$  with ~10 % (EL1 + Rhodium protective layer) or up to 35 % (EL1 + protective nano-coating). However, the importance of protective layers becomes visible in the environmental tests; an 85 % decrease of the equivalent conductivity in Ku-band was detected for pure electroless silver surface (EL1) in a salt-frog test (from 6.2 to 1.2 S/m [A57]), while the protected with Rd surface keeps value  $\sigma_{eq} \sim 4.3$  S/m. Similar measurements allow us to establish the acceptable equivalent conductivity for metalized injection-moulded or 3D printed plastics with metallization; the calculated attenuation ~1 dB/m in WR28 waveguide for Ka-band can be satisfied for mean  $\sigma_{eq} \geq 2.5$  S/m (at 32 GHz) – see the dependencies in Fig. 6.4*b*.

## 6.2. EQUIVALENT CONDUCTIVITY OF BOTH SIDES OF METALIZATION USED FOR REINFORCED COMMERCIAL SUBSTRATES

The determination of equivalent conductivity of copper metallization used for the microwave substrates is extremely important especially because the producers apply Cu folio with different roughness of both sides [43]. In the considered in the previous section waveguide components made from metalized plastics, the losses depend on the equivalent conductivity  $\sigma_{eq}$  of the metallization top surface. Contrariwise, this role for the substrate metallization is playing from the bottom side (to the substrate) and strongly determines the transmission-line losses of printed planar structures, especially in the mm-wavelength range [44]. To minimize these losses, but to ensure acceptable adhesion of the metallization to the substrate surface, the producers apply different techniques to increase the roughness of the bottom surface, which decrease the equivalent conductivity. Our method [A57] allows accurate distinguishing of this difference – see the measured dependencies of the top and bottom sides' conductivity  $\sigma_{eq}$  for several realistic Cu folios in Fig. 6.5*a*; the top surface has typically 3-5 times higher  $\sigma_{eq}$ , excepting reverse treated substrates. The reasons are well explainable. The standard technology for electro-deposited (ED) Cu folio ensures typically RMS irregularity  $R_{RMS} \sim 0.3\text{-}0.4$   $\mu\text{m}$  (which better represents the surface roughness RGH) of the metal top surface (drum or resists side), while the values for the opposite backside are  $R_{RMS} \sim 1\text{-}4$   $\mu\text{m}$  [43]. Only by R/A (rolled/annealed) techniques, these values can be decreased to  $R_{RMS} \sim 0.4$   $\mu\text{m}$ . The producers verified the obtained volume and surface resistivity by the IPC-TM-650 2.5.17.1 test method [45] at low frequencies. Our measurement method allows more reliable characterization of the equivalent conductivity of both metallization sides at the actual working frequencies. Fig. 6.5*b* shows the measured attenuation of two commercial substrates with Dk ~3 with ED and LoPro®

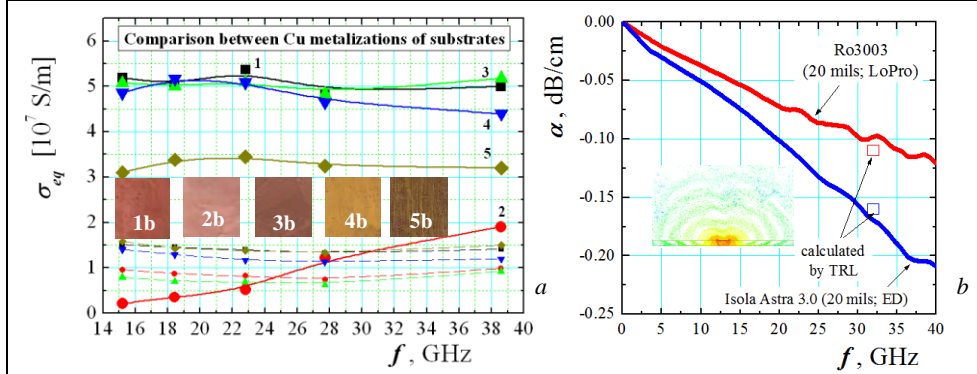
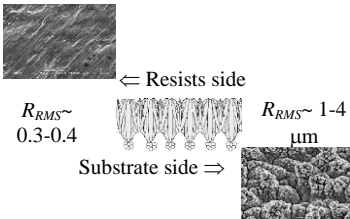


**Fig. 6.5.** *a)* Measured equivalent conductivity of copper metallization for microwave substrates; top/resist (solid curves) and bottom (dashed curves) sides (17.5- $\mu\text{m}$  thick Cu folio). Legend: 1 – Rolled/Annealed (R/A,  $R_{RMS} = 0.4 \mu\text{m}$ ); 2 – Reverse Treated (RTF); 3, 4 – Electro-Deposited ED with different adhesive glue; 5 – ED, additionally electro-plated (35- $\mu\text{m}$  thick). The pictures present the images of the bottom surfaces (to the substrate); *b)* Attenuation in 50-Ohms microstrip line on substrates with ED or LoPro® metallization, calculation by measured  $\sigma_{eq}$  (see Table 14)

**Table 14.** Measured equivalent conductivity  $\sigma_{eq}$  of the Copper folio for microwave substrates and calculated conductor and total losses in 50-Ohms MSL (insets: RGH of both metallization sides).

Metal type (RGH $R_{RMS}$ )	$\sigma_{eq}$ , S/m	$\alpha_c$ , dB/cm (conductor only)	$\alpha_{tot}$ , dB/cm
Ideal Cu	$5.80 \cdot 10^7$	0.041	0.065
R/A (0.4 $\mu\text{m}$ )	$5.09 \cdot 10^7$	0.044	0.067
ED LoPro (0.9 $\mu\text{m}$ )	$1.37 \cdot 10^7$	0.084	0.112
ED (2.0 $\mu\text{m}$ )	$0.63 \cdot 10^7$	0.113	0.161
RTF (1.8 $\mu\text{m}$ )	$0.79 \cdot 10^7$	0.110	0.138



metallization and calculated values at 32 GHz for the same cases by TRL calculators. The rolled/annealed (R/A) metallization used for substrates in the mm-wavelength range has better  $\sigma_{eq}$  ( $\sim 1.5 \times 10^7$  S/m) in comparison to the electro-deposited metallization ( $\sim 0.7 \times 10^7$  S/m) (Fig. 6.5a), which ensure attenuation decrease from 0.16 dB/cm to  $\sim 0.11$  dB/cm (Fig. 6.5b; Table 14).

### 6.3. EQUIVALENT CONDUCTIVITY OF METASURFACES AND MATERIALS WITH LOW CONDUCTIVITY

The proposed in [A57] method for accurate characterization of equivalent conductivity even for values less than  $\sigma_{eq} < 10^5 \div 10^1$  S/m is fully applicable for different metasurfaces and materials with low conductivity. A good test of the used measurement resonators is the characterization of carbon-based samples. Fig. 6.6a shows how the measurement resonators with high Q factors allow reliable  $\sigma_{eq}$ -measurements of carbon-based samples (ordinary or carbon nanotube CNT cloths with epoxy); the CNT samples have 10 times higher  $\sigma_{eq} \sim (0.2-1) \times 10^5$  S/m instead  $\sim (0.4-1) \times 10^4$  S/m. The conductivity of the textile fabrics with different conductive fibres content is also well determinable  $\sim 10^4-5 \cdot 10^5$  S/m. Very successful could be the  $\sigma_{eq}$  characterization of meta-surfaces – a

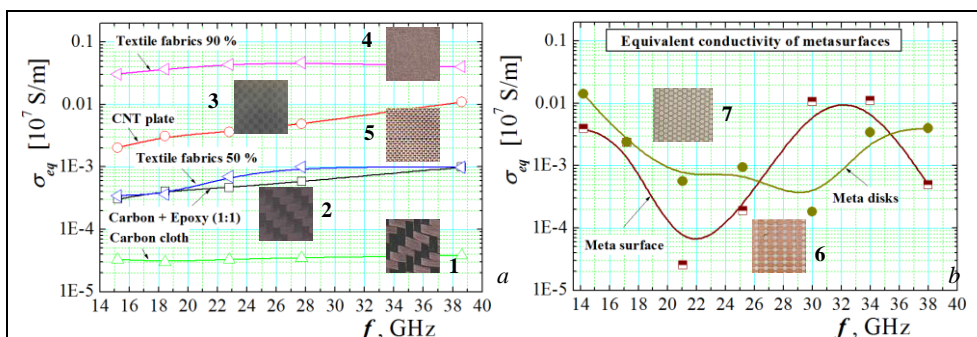


**Fig. 6.6.** *a)* Measured equivalent conductivity of low-conductive samples. Legend: 1 – pure Carbon cloth; 2 – Carbon cloth + epoxy (1:1); 3 – CNT cloth + epoxy; 4, 5 – conductive textile fabrics (90% and 50 % conductive fiber content); *b)* 6 – artificial metasurface; 7 – meta disks

possible resonance/periodical conductivity behaviour is fully detectable and measurable for the already considered metasurface samples (compare with the dependencies for the resonance behaviour of dielectric constant in Fig. 5.1*b*).

## 7. CONCLUSIONS

In this paper, we summarize the main results from our 18-year work devoted to the characterization of the dielectric properties of materials used in modern microwave electronics. In the first part, we prove the assumption that the well-determined complex dielectric and magnetic constants of the materials are important not only for improving the accuracy of the modern 3D design of nowadays electro-dynamic structures but also because the integral character of these parameters ensures valuable information for the real material composition, structure, character of inclusions, building blocks and unit cells orientation, used technology, conditions for the material preparation, etc. We have shown that additional very useful information can be achieved when the actual anisotropy of the material constants has been determined and compared – different behaviour of their permittivity/permeability in different directions. Our numerical models and experimental methods for characterization of the sample dielectric and magnetic properties including their anisotropy give satisfactory accuracy practically for all possible applications. The full set of the implemented resonance and broadband measurement methods in our Microwave laboratory gives us the possibility for deep investigation and characterization of a variety of different materials in the nowadays electronics – microwave substrates, ceramics, multilayer composites, different dielectric mixtures, 3D printed dielectrics, textile fabrics, metamaterials, thin micro- and nano-films, carbon-content materials, fresh and dry plant tissues, etc.

**Acknowledgements.** The investigations have been supported by the Bulgarian National Scientific Found under Contract No. DN-07/15/2018-19 and partially under Contract No. КП-06-Индия-7/2019 (for bent and anisotropic

antenna patches and resonators and wearable antennas with metamaterials).

#### REFERENCES

- [1] P. I. Dankov (2019), *Annuaire de l'Université de Sofia "St. Kliment Ohridski", Faculté de Physique*, v. 112 (this issue; part 1)
- [2] E. Tuncer (2013), "Dielectric Mixtures – Importance and Theoretical Approaches", *IEEE Electrical Insulation Magazine*, April 2013, DOI: 10.1109/MEI.2013.6648753
- [3] A. Sihvola (1999), "Electromagnetic Mixing Formulas and Applications", The Institute of Electrical Engineers, *Electromagnetic Waves Series 47*, London, UK
- [4] K. Bal, V. K. Kothari (2010), "Permittivity of Woven Fabrics: A Comparison of Dielectric Formulas for Air-Fiber Mixture", *IEEE Transactions on Dielectrics and Electrical Insulation*, vol. 17, No. 3; pp. 881-889
- [5] Z. Li, A. Haigh, C. Soutis, A.A.P. Gibson (2018), "X-band microwave characterization and analysis of carbon fibre-reinforced polymer composites", *Composite Structures*, 208, DOI: 10.1016/j.compstruct.2018.09.099
- [6] Z. Li, A. Haigh, C. Soutis, A. Gibson, R. Sloan (2017), "Dielectric constant of a three-dimensional woven glass fibre composite: analysis and measurement", *Composite Structures, Elsevier B.V.*, Vol. 180, pp. 853-861
- [7] E. Tuncer, Y.V. Serdyuk, S.M. Gubanski (2002), "Dielectric mixtures: electrical properties and modeling", *IEEE Trans. on Dielectrics and Electrical Insulation*, Vol. 9, Issue: 5, pp. 809-828, DOI: 10.1109/TDEI.2002.103866
- [8] IPC TM-650 2.5.5.5 (1998) Test Methods Manual, <http://www.ipc.org/html/fsstandards.htm>
- [9] FR-4 Datasheets; <http://www.alldatasheet.com/datasheet-pdf/pdf/458178/FREESCALE/FR4.html>
- [10] Rogers Corp datasheet: <https://www.rogerscorp.com/acs/products/45/RO3203-RO3206-and-RO3210-Laminates.aspx>
- [11] S. J. Normyle (2006), Application Note: The Anisotropy Of Dielectric Constant (Er) In TLY-5A Material By Bereskin", *Microwave Journal, Wireless Design Online* ([http://www.taconic-add.com/pdf/technicalarticles--anisotropy\\_of\\_dielectric\\_constant\\_in\\_tly5a\\_material.pdf](http://www.taconic-add.com/pdf/technicalarticles--anisotropy_of_dielectric_constant_in_tly5a_material.pdf))
- [12] A. B. Bereskin (1992), "Microwave test fixture for determining the dielectric properties of the material", US Patent 50083088, Jan. 1992
- [13] A. F. Horn III, P. A. LaFrance, J. W. Reynolds, and J. Coonrod (2012), "The influence of test method, conductor profile and substrate anisotropy on the permittivity values required for accurate modeling of high frequency planar circuits." *Circuit World* 38, no.4, 2012, pp. 219-231
- [14] J. Coonrod (2015), "Critical Aspects of Dielectric Constant Properties for High Frequency Circuit Design", *Microwave Journal, Web Seminar, Online: www.microwavejournal.com/WebinarSlides\_9dec15*
- [15] R. Salvado et. al. (2012), "Textile Materials for the Design of Wearable Antennas: A Survey", *Sensors* 2012, vol. 12, pp. 15841-15857; ISSN 1424-8220; doi:10.3390/s121115841
- [16] D. T. Paris (1970), *IEEE Trans. on Antennas and Propagation*, AP-18, pp. 7-15, Jan. 1970
- [17] J. Krupka (2006), *IoP Publishing, Meas. Sci. Technol.* 17 R55–R70 doi:10.1088/0957-0233/17/6/R01
- [18] S. A. Ivanov, K. V. Bachev (1984), *Bulg. J. Phys.* 11, 1984, pp. 513-519
- [19] P. R. Andrade, and S. P. S. Porto (1974), *Annual Review of Materials Science*, 4, 287  
<https://doi.org/10.1146/annurev.ms.04.080174.001443>
- [20] L. F. Chen, C. K. Ong, C. P. Neo, V. V. Varadan, V. K. Varadan (2004), *Microwave Electronics: Measurement and Materials Characterization*, John Wiley & Sons Ltd., England, Ch. 5/8
- [21] V. G. Harris (2012), *IEEE Trans. on Magnetics* 48 No. 3 1075-1104
- [22] C.R. Garcia et. al. (2012), "3D Printing of Anisotropic Metamaterials", *PIERS Letters*, vol. 34, pp. 75-82
- [23] M. Liang, W.-R. Ng, K.Chang, M.E.Gehm, and H. Xin(2011), "An X-Band Luneburg Lens Antenna Fabricated by Rapid Prototyping Technology", *IEEE MTT-S Digest (MTT)*, DOI: [10.1109/MWSYM.2011.5972738](https://doi.org/10.1109/MWSYM.2011.5972738)
- [24] J. Budhu, Y. Rahmat-Samii, R.E. Hodges, D.C. Hofmann, D.F. Ruffatto, K.C. Carpenter (2018), "3D-Printed Shaped Engineered Material Inhomogeneous Lens Antennas for Next Generation Spaceborne Weather Radar Systems", *IEEE Antenna and Wireless Prop. Letters*, v.17, No.11, DOI:[10.1109/LAWP.2018.2848263](https://doi.org/10.1109/LAWP.2018.2848263)
- [25] J. Y. Cassivi, Ke Wu (2004), Substrate integrated nonradiative dielectric waveguide, *IEEE Microwave and Wireless Components Letters*, Vol. 14, issue 3, DOI: 10.1109/LMWC.2004.824808
- [26] S. Rondineau, M. Himdi and J. Sorieux (2003), "A Sliced Spherical Luneburg Lens", *IEEE Antennas and Wireless Propagation Letters*, vol. 2, pp. 163-166, Feb. 2003
- [27] M. I. Menzel et. al. (2009), Non-invasive determination of plant biomass with microwave resonators; *Plant, Cell and Environment* 32 (2009), 368-379, doi: 10.1111/j.1365-3040.2009.01931.x
- [28] V.A. Sydoruk et. al. (2016), Design and Characterization of Microwave Cavity Resonators for Noninvasive Monitoring of Plant Water Distribution, *IEEE Trans. Microw. Theory Tech.*, MTT-64, No. 9, 2894-2904
- [29] W.X. Jiang, J.Y. Chin and T. J. Cui (2009), "Anisotropic metamaterial devices", *Materials Today*, vol. 12, No. 12, Dec. 2009, pp. 26-33
- [30] European Commission (Directorate-General for Research, Communication Unit), Nano-structured Metamaterials, B-1049 Brussels, online: <http://ec.europa.eu/research/research-eu>
- [31] H. O. Ali (2017), "Review of porous anodic aluminium oxide (AAO) applications for sensors, MEMS and

biomedical devices,” *Int. Journal of Surface Engineering and Coatings* 95 (6), 290-296

[[doi.org/10.1080/00202967.2017.1358514](https://doi.org/10.1080/00202967.2017.1358514)]

[32] A. M. Md Jani, D. Losic and N. H. Voelcker (2013), “Nanoporous anodic aluminium oxide: Advances in surface engineering and emerging applications,” *Progress in Materials Science* 58, 636–704 (2013)

[<http://dx.doi.org/10.1016/j.pmatsci.2013.01.002>]

[33] M. Dragoman et al. (2013), “The electromagnetic properties of Graphene in the microwave and millimeter-wave spectrum”, *Proc. 43rd EuMC*, 7-10 Oct 2013, Nuremberg, Germany, pp. 530-532

[34] E. Valcheva, K. Kirilov, B. Arnaudov, N. Bundaleska, J. Henriques, S. Russev, and E. Tatarova (2019),

“Electrical conductivity of free-standing N-graphene sheets”, *AIP Conference Proceedings* **2075**, 160038 (2019), <https://doi.org/10.1063/1.5091365>

[35] R. B. Piejak, J. Al-Kuzee, and N. St. J. Braithwaite (2005), “Hairpin resonator probe measurements in RF plasmas”, *Plasma Sources Sci. Technol.*, 14, pp.734-743

[36] C. Scharwitz, M. BoËke, J. Winter (2008), “Optimised Plasma Absorption Probe for the Electron Density Determination in Reactive Plasmas”, *Plasma Process. Polym.* 2008, 5

[37] Andrew L. Goodyear, Mark Dineen, and Ligang Deng (2002), “A Comparison of Production Plasma Etch Chemistries for InP and Related Materials”, © Oxford Instruments 2002, Oxford Instruments Plasma Technology (online available)

[38] A. S. Tatarenko and M. I. Bichurin (2012), “Microwave Magnetolectric Devices”, *Advances in Condensed Matter Physics*, V. 2012, Hindawi Publishing Corporation, ID 286562, doi:10.1155/2012/286562

[39] K. Ebnabbasi, Y. Chen, A. Geiler, V. Harris, and C. Vittoria (2012), “Magneto-electric effects on Sr Z-type hexaferrite at room temperature”, *J. of App. Phys.*, 111, 2012, doi: 10.1063/1.3678588

[40] A. El Fellahi, A. Mazzamuro, J. C. Gerbedoen, Y. Dusch, O. B. Matar, P. Pernod, A. Talbi, and N. Tiercelin (2018), “Miniaturized Coplanar Waveguide for Nanostructured Magnetostrictive Multilayer Characterization”, *MDPI Proceedings* 2018, 2, 851; doi:10.3390/proceedings2130851

[41] A. M. Fowler (1970), “Radio Frequency Performance of Electroplated Finishes”, *Proc. IREE Australia*, May 1970, pp. 148-164

[42] Spray metallization by 2 aerosols in aqueous phase: <https://www.jetmetal-tech.com/technologies?lang=en>

[43] “Copper Foils for High Frequency Materials” (2019), Advanced Connectivity Solutions, Rogers Corp. Chandler, AZ 85226 [www.rogerscorp.com](http://www.rogerscorp.com)

[44] Allen F. Horn III, Patricia A. LaFrance, Christopher J. Caisse, John P. Coonrod, Bruce B. Fitts (2016), “Effect of conductor profile structure on propagation in transmission lines,” *DesignCon2016*

[45] IPC-TM-650 2.5.17.1 Test method “Volume and Surface Resistivity of Dielectric Materials” (metallic-clad laminates)

#### AUTHORS' REFERENCES

[A3] S. A. Ivanov and P. I. Dankov (1995), *Proc. ISRAMIT'95*, Kiev, Ukraine, pp. 574-577

[A4] P. I. Dankov (1996), *Proc. 13<sup>th</sup> Int. Conf. on Microwave Ferrites*, Romania, pp. 21-27

[A5] P. I. Dankov, S. A. Ivanov (1997), *Annuaire de l'Université de Sofia “St. Kliment Ohridski”*, Faculté de physique, 91, 1997, pp. 5-31

[A6] S. A. Ivanov and P. I. Dankov (1998), *Proc. 7<sup>th</sup> Int. Conf. on Mathematical Methods on Electromagnetic Theory*, Kharkov, Ukraine, pp. 378-380

[A7] P. I. Dankov (1998), *Proc. 14<sup>th</sup> Int. Conf. on Microwave Ferrites*, Hungary, pp. 166-170

[A8] S.A. Ivanov, P.I. Dankov (2000), *2<sup>nd</sup> International Symposium of Trans Black Sea Region Applied Electromagnetism*, : Xanthi, Greece, DOI: 10.1109/AEM.2000.943254

[A9] V. Peshlov, I. Slavkov, and P. Dankov (2001), *Proc. EuMC'2001*, vol. 3, London, UK, pp. 257-260

[A10] M. Gatchev, S. Kamenopolsky, V. Boyanov, P. Dankov (2002), *14<sup>th</sup> MIKON'2002*, Gdansk, Poland, pp. 189-192

[A11] J. Bozmarov, R. Traykov, V. Peshlov, P. Dankov (2002), *14<sup>th</sup> MIKON'2002*, Gdansk, Poland, DOI: 10.1109/MIKON.2002.1017986

[A12] S.A. Ivanov and P.I. Dankov (2002), *J. Electrical Engineering*, vol. 53, No. 9s, pp. 93–96

[A12a] S.A. Ivanov, P.I. Dankov (2000), *Proc. of the 2nd Int. Symposium of Trans Black Sea Region on Applied Electromagnetism* (Cat. No.00TH8519), 29-29 June 2000, Xanthi, Greece. DOI: 10.1109/AEM.2000.943254

[A13] P. Dankov, S. Kamenopolsky, V. Boyanov (2003), *14<sup>th</sup> Microcoll'2003*, Budapest, Hungary, pp.217-220

[A14] P. I. Dankov (2004), *15<sup>th</sup> MIKON'2004*, Warsaw, Poland, May 2004, vol. 1, pp. 151-154

[A15] V. Peshlov, S. Alexandrov and P. Dankov (2004), *15<sup>th</sup> MIKON'2004*, Warsaw, Poland, v. 2, pp. 562-566

[A16] P.I. Dankov, S.M. Kolev, S.A. Ivanov (2004), *17<sup>th</sup> EMFM-2004*, Warsaw, Poland, pp. 89-93

[A17] I. Nedkov, S. Kolev, P. Dankov, S. Alexandrov (2004), *Proc. IEEE Int. Spring Seminar on Electronics Technology 27<sup>th</sup> ISSE 2004*, Sofia, Bulgaria, pp. 577-579

[A18] P. I. Dankov, and S. A. Ivanov (2004), *34<sup>th</sup> EuMC'2004*, Amsterdam, Holland, pp. 753-756

- [A19] P. I. Dankov, V. P. Levcheva, and V. N. Peshlov (2005), *35<sup>th</sup> EuMC'2005*, Paris, France, pp. 515-519
- [A20] V. N. Peshlov, P. I. Dankov, B. Hadjistamov (2005), *1<sup>st</sup> European Conference on Antennas and Propagation EuCAP'2005*, France, Nice, No. 349840PD (available IEEE Xplore)
- [A21] P. I. Dankov, B. Hadjistamov, and V. P. Levcheva (2006), *Proc. IVth Mediterranean Microwave Symposium (MMS'2006)*, Genoa, Italy, Sept. 19-21, 2006 (available IEEE X-plore)
- [A22] P. I. Dankov (2006), *IEEE Trans.on MTT*, vo. 54, no.4, pp. 1534-1544
- [A23] B. N. Hadjistamov, V. P. Levcheva, and P. I. Dankov (2007), *Proc. Vth Mediterranean Microwave Symposium (MMS'2007)*, Budapest, Hungary, pp. 183-186
- [A24] P. I. Dankov, V. P. Levcheva, and I. I. Arestova (2007), *Proc.ICMF'2007*, Budapest, Hungary, pp.27-30
- [A25] P. I. Dankov and B. Hadjistamov (2007), *37<sup>th</sup> EuMC'2007*, Munich, Germany, pp. 933-936
- [A26] P. I. Dankov, V. N. Peshlov, M. Gachev (2008), *30<sup>th</sup> ESA Antenna Workshop on Antennas for Earth Observation, Science, Telecommunications and Navigation Space Missions*, Noordwijk, The Netherlands, pp. 505-508 (invited COST paper)
- [A27] V. P. Levcheva, B. N. Hadjistamov, P. I. Dankov (2008), *Bulg. J. Phys.*, 35, pp. 33-52
- [A28] P. Dankov, P. Stefanov, V. Gueorguiev, T. Ivanov (2008), *J. of Physics*, Conf. Series, pp. 202-209
- [A29] V. P. Levcheva, I. I. Arestova, B. R. Nikolov, and P. I. Dankov (2009), *Telfor Journal*, Vol. 1, No. 2, 2009, pp. 57-60
- [A30] S. R. Baev, B. N. Hadjistamov, and P. I. Dankov (2009), "Lüneburg Lenses as Communication Antennas", *Annuaire de l'Universite de Sofia "St. Kliment Ohridski", Faculte de Physique*, 102, 2009, pp. 67-84
- [A31] P. Dankov, B. N. Hadjistamov, I. Arestova, V. Levcheva (2009), *PIERS online*, vol. 5, no. 6, pp.501-505
- [A32] P. I. Dankov (2010), "Dielectric Anisotropy of Modern Microwave Substrates", *Chapter 4 in "Microwave and Millimeter Wave Technologies from Photonic Bandgap Devices to Antenna and Applications"*, ed. by Igor Minin, In-Tech Publ., Austria, Jan. 2010, ISBN 978-953-7619-66-4
- [A33] P. I. Dankov, M. I. Kondeva, and S. R. Baev (2010), ISBN: 978-1-4244-4883-8, *iWAT Conference*, Lisbon, Portugal, DOI 10.1109/IWAT.2010.5464930 (online IEEE Xplore)
- [A34] K. Zlatkov, P. Dankov (2011), *Microwave Review*, ISSN 14505835, UDK 621.3.049.77, pp. 29-35
- [A35] B. N. Hadjistamov, P. I. Dankov (2011), *Bulg. J. Phys.* 38, pp. 191-198
- [A36] P. Dankov, Z. Kiss'ovski (2012), *XXI ESCAMPIG*, Viana do Castelo, Portugal
- [A37] P. I. Dankov (2013), *2<sup>nd</sup> National Congress on Physical Sciences*, Sofia, Bulgaria (online)
- [A38] P. I. Dankov (2014), *J. of Physics: Conf. Series 516*, DOI:10.1088/1742-6596/516/1/012001
- [A39] R. B. Borisov, K. I. Zlatkov, and P. I. Dankov (2014), *E+E Journal*, vol. 49, No. 3-4, 2014, pp. 7-12
- [A40] M. Gachev, V. Boyanov, S. Kamenopolsky, V. Peshlov, B. Marinov, and P. Dankov (2014), DOI: 10.1109/EuCAP.2014.6902312, *8<sup>th</sup> EuCAP'2014*, The Hague, The Netherlands, (online)
- [A41] M. Gachev, P. Dankov (2015), *8<sup>th</sup> Management Committee Meeting and Workshop*, Sofia, Bulgaria
- [A42] P. Dankov, V. Peshlov, and T. Amla (2015), *8<sup>th</sup> Management Committee Meeting and Workshop*, Sofia, Bulgaria, Sofia University, Aula Magna. (online available)
- [A43] P. Dankov, S. Kamenopolski, V. Peshlov, R. Traykov (2016), *9<sup>th</sup> GSMM2016 7th ESA Workshop on Millimetre-Wave Technology and Applications*, Espoo, Finland (IEEE Xplore)
- [A44] P. I. Dankov (2016), *EuMC'2016*, London, UK, pp. 158-161
- [A45] M. Gachev, and P. Dankov (2016), NSS-07-0601, *7th Nano-Satellite Symposium and 4th Unisec-Global Meeting*, Kamchia, Bulgaria, 2016 (online available)
- [A46] P. I. Dankov (2017), *iWAT'2017*, Athens, Greece, pp.61-64 (IEEE Xplore)
- [A47] P. I. Dankov (2017), *FERMAT*, Vol. 22, Communication 9, ISSN 2470-4202 (see [A46])
- [A48] P. I. Dankov (2017), *Proc. IEEE MTT-S Int. Conf. NEMO'2017*, DOI: 10.1109/NEMO.2017.7964199
- [A49] P. I. Dankov (2017), *Proc. IEEE MTT-S Int. Microwave Workshop Series on Advanced Materials and Processes*, Pavia, Italy, (IEEE Xplore)
- [A50] P. I. Dankov (2017), *Proc. 47<sup>th</sup> EuMC'2017*, Nurenburg, Germany, pp. 954-957 (online)
- [A51] P. I. Dankov, M. I. Tsatsova, and V. P. Levcheva (2017), *Proc. of PIERS'2017*, Singapore
- [A52] P. I. Dankov, and I. I. Iliev (2017), *Proc. of PIERS'2017*, Singapore
- [A53] P. I. Dankov (2018), *8<sup>th</sup> Int. Workshop and Summer School on Plasma Physics (IWSSPP'2018)*, Kiten, Bulgaria, (invited paper; online); *Journal of Physics: Conf. Series*, IOP Publishing, 2019
- [A54] P. I. Dankov (2018), *Proc. 48<sup>th</sup> EuMC*, Madrid, Spain, (IEEE Xplore)
- [A55] V. Levcheva, P. Dankov (2018), *Bulg. J. Phys.*, v. 45, pp. 264-274
- [A56] P. Dankov, V. Levcheva, M. Iliev (2018), *Proc. Metamaterials'2018*, Espoo, Finland, online
- [A57] P. Dankov, R. Traykov, V. Peshlov, and S. Kamenopolski (2018), *Asia-Pacific Microwave Conference APMC2018*, Kyoto, Japan, (IEEE Xplore)
- [A58] P. I. Dankov, M. T. Iliev, V. P. Levcheva (2018), *Bulgarian Chemical Communications*, Vol. 50 (Special Issue F), pp. 126-134
- [A59] M. Gachev, and P. Dankov (2019), „Microwaves in Bulgaria”, *1<sup>st</sup> European Microwave Conference in*

*Central Europe, Prague, Czech Republic, IEEE Xplore (online)*

[A60] P. Dankov; B. Tzaneva; V. Videkov (2019), SPIE Conference Proceeding, Proceedings Volume 11332, International Conference on Quantum, Nonlinear, and Nanophotonics 2019 (ICQNN 2019) (online)

[A61] P. I. Dankov (2019), *IEEE 19th Mediterranean Microwave Symposium*, Tunisia, Nov.2019 IEEE Xplore

[A62] P. Dankov, S. Kolev, T. Koutzarova (2019), VIET2019, Sept. 2019, Sozopol, Bulgaria, Journal of Physics: Conf. Series, IOP Publishing 2020 (online)

[A63] P. Dankov, V. Levcheva, S. Kolev, and T. Koutzarova (2019), VIET2019, Sept. 2019, Sozopol, Bulgaria, Journal of Physics: Conf. Series, IOP Publishing 2020 (online)

[A64] P. Dankov, V. Levcheva, P. Sharma (2020), iWAT2020, Feb. 2020, Bucharest, Romania (IEEE Xplore)

[A65] P. Dankov (2020), "Anisotropy of artificial materials and how to characterize it?" - COST Action CA18223 SyMat Meeting – Prague, Feb. 2020 (online)

[A66] P. Dankov (2020), "Material Characterization in the Microwave Range – another look to the properties of modern artificial dielectrics", (invited lecture; 10th International Advances in Applied Physics & Materials Science Congress & Exhibition (APMAS2020), October 14-20, 2020, Oludeniz, Turkey (to be published in ACTA Materialia Turcica)

[A67] V. Levcheva, and P. Dankov (2020), "Characterization of Microwave Absorbers, Including Multilayer Nanoabsorbers", 22nd International Conference Materials, Methods & Technologies, 29 Aug. – 1 Sept. 2020, Burgas, Bulgaria (to be published in Materials, Methods & Technologies; ISSN 1314-7269)

[A68] P. Dankov, and V. Levcheva (2020), "Investigations of Artificial Metamaterials and Multilayer Nano-Composites in External Magnetic Field", 22nd International Conference Materials, Methods & Technologies, 29 Aug. – 1 Sept. 2020, Burgas, Bulgaria (to be published in Materials, Methods & Technologies; ISSN 1314-7269)